Icarus 463 (2027) 117372

Contents lists available at ScienceDirect

Icarus

journal homepage: www.elsevier.com/locate/icarus

Chronology and composition of lunar mare basalts in Maria Undarum and Spumans

Jingdong Zhang [a,b], Yuzheng Zhang [a], Jian Chen [a], Luyuan Xu [c,b], Le Qiao [a,b,*]

[a] Shandong Key Laboratory of Space Environment and Exploration Technology, School of Space Science and Technology, Institute of Space Sciences, Shandong University, Weihai, Shandong 264209, China
[b] State Key Laboratory of Lunar and Planetary Sciences, Macau University of Science and Technology, Macau, China
[c] International Institute for Interdisciplinary and Frontiers, Beihang University, Beijing 100191, China

ARTICLE INFO

Keywords:
Maria Undarum and Spumans
Mare basalt
Chronology
Crater size-frequency distribution
Moon

ABSTRACT

Investigations of the ages and compositions of lunar volcanic deposits provide insights into the geologic and thermal evolution of the Moon. Among the 22 recognized lunar maria, the majority have been chronologically studied, and Maria Undarum and Spumans remain the two major maria that lack reliable age constraints. In this work, 66 undated mare basalt units were delineated in the two maria and adjacent regions. Our analysis reveals that the absolute model ages (AMAs) of these 66 basalt units range from 2.9 to 3.8 Ga. Additionally, noticeable heterogeneity in surface composition is observed among these mare units. Combining characteristics of regional volcanic flux and mare composition, we suggest a gradual decline in volcanic activity after the main phase of volcanism, with older units (3.8–3.5 Ga) generally exhibiting greater exposed basalt volumes than younger units (3.4–2.9 Ga). The AMAs of these maria show weak negative correlations with their surface FeO and TiO_2 abundances, although neither relationship is statistically significant. Younger basalts are dominated by relatively lower titanium contents and have a narrower variety in iron contents than older basalts. Furthermore, we constrain the lower limit of the basalt thickness in this region, ranging from ~41 m to 207 m. Systematic investigation of the age, composition, basalt thickness, and volumetric flux of the Maria Undarum and Spumans region demonstrates that small-scale volcanic eruptions outside major impact basins are generally very ancient (>3.5 Ga), and are characterized by short durations, irregular mare outlines, small eruptive volumes, and emplacement in depressions in highland terrains.

1. Introduction

Unlike terrestrial planets, the Moon stands out for its characteristic size and bulk density, providing essential insights into the thermal evolution of an endmember within the spectrum of differentiated planetary bodies (Hiesinger and Head, 2006; Shearer et al., 2006). Lunar volcanism is a key endogenic process that provides important insights into the Moon's geological history and thermal evolution (Head and Wilson, 1992; Head et al., 2023). Lunar mare basalts, which are the most prevalent volcanic features on the Moon, cover approximately 17% of its total surface area (Head, 1976). Accurate estimates of mare basalt ages are necessary to constrain the duration and flux of lunar volcanism. Additionally, they provide essential insights into the petrogenesis of lunar mare basalts and their connection to the Moon's thermal evolution (Hiesinger et al., 2011a).

Studies of lunar basalt samples brought back by the Apollo and Luna missions have accurately established that volcanism on the Moon could date back to as early as 3.9 Ga and continued until at least 3.1 Ga (Head, 1976; Stöffler et al., 2006; Nyquist and Shih, 1992; Righter and Drake, 2000; Snape et al., 2019). These findings are of great significance as they provide indispensable reference points for a comprehensive examination of the lunar volcanic history and thermal evolutionary processes (Nyquist and Shih, 1992; Basilevsky et al., 2010). Subsequent analysis of returned lunar samples and meteorites extended the known duration of lunar volcanism. The basaltic samples from the Chang'e-5 mission yield a crystallization age of approximately 2.03 Ga and those from the Chang'e-6 lunar farside sample return mission are dated at 2.8 Ga (Li et al., 2021; Che et al., 2021; Zhang et al., 2025). Terada et al.

* Corresponding author at: Shandong Key Laboratory of Space Environment and Exploration Technology, School of Space Science and Technology, Institute of Space Sciences, Shandong University, Weihai, Shandong 264209, China.
E-mail address: leqiao@sdu.edu.cn (L. Qiao).

https://doi.org/10.1016/j.icarus.2026.117372
Received 9 April 2026; Received in revised form 10 October 2026; Accepted 1 November 2026
Available online 3 November 2026
0019-1035/© 2026 Elsevier Inc. All rights are reserved, including those for text and data mining, AI training, and similar technologies.

(2007) reported a 4.35 Ga age for lunar meteorite Kalahari 009, representing one of the oldest known volcanic rocks from the Moon. Borg et al. (2004) reported a crystallization age of ~2.87 Ga for lunar meteorite NWA (Northwest Africa) 773, extending the recognized duration of lunar KREEP (a lunar geochemical component enriched in potassium, rare earth elements, and phosphorus) magmatism by approximately 1 billion years beyond the traditionally accepted timeframe of 3.8–4.6 Ga. Recent analysis of the lunar basaltic meteorite NWA 16286 revealed a KREEP-rich basaltic eruption 2.2 Ga ago, offering fresh insights into the mechanisms that sustained prolonged volcanic activity on the Moon (Yang et al., 2025).

Nevertheless, it should be emphasized that these precise sample age measurements are only representative of a limited number of specific locations on the lunar surface. Fortunately, remote-sensing techniques, particularly the crater size–frequency distribution (CSFD) measurements, enable us to estimate both relative and absolute model ages for regions of the Moon that have not been sampled (Neukum et al., 2001; Hiesinger et al., 2003). The CSFD method has been employed to accurately date the majority of 22 lunar maria ages (~500 basaltic units; e.g., Cho et al., 2012; Haruyama et al., 2009; Hiesinger et al., 2006, 2011a, 2011b; Morota et al., 2009, 2011; Pasckert et al., 2015, 2018; Jin et al., 2025). The results indicate that model ages of mare basalts range from ~1.5 Ga to 4.0 Ga, with most basaltic units dated between 3.5 Ga and 3.7 Ga and a prominent concentration of ages around 3.5 Ga. Among all the 22 named lunar maria (lunar mare regions with International Astronomical Union (IAU) officially recognized names; Andersson and Whitaker, 1982), only three maria, i.e., Maria Undarum and Spumans in the southeast of Mare Crisium and Mare Anguis in the north of Mare Crisium, remain undated (Fig. 1), largely due to their small sizes and the low resolution of early data sets. Moreover, unlike large mare basalt deposits within lunar impact basins, which commonly occur in topographic lows associated with thin crustal regions, Maria Undarum and Spumans are situated along the exterior of the Crisium multi-ring basin, where the terrain is topographically elevated and the crust is expected to be thicker. This distinct geological setting enables comparisons between volcanic processes occurring within and outside large impact basins, providing new insights into how basin-related crustal structures and crustal thickness variations influenced localized mare basalt emplacement and the broader volcanic evolution of lunar basins.

In this work, we systematically investigated the CSFD-derived absolute model ages (AMAs), surface compositional variations, mineralogy, lower-limit estimates of exposed basalt thickness, and volume of the basalt units in Maria Undarum and Spumans and surrounding regions. We identified and delineated 66 basaltic units on the basis of their topographic, spectral, and compositional signatures. Absolute model ages for each unit were subsequently derived through CSFD measurements. We also conducted a detailed analysis of the FeO and TiO_2 composition of all 66 basaltic units. Using the impact crater excavation depth method, we estimated the basalt thicknesses of these mare units and calculated the cumulative lava flux over the study region. We also examined the potential correlation between mare thickness and eruption age. On the basis of the temporal evolution of both eruption flux and compositional signatures, we identify a gradual decline in volcanic activity in the study area after the main phase of volcanism. Although relatively small in size, the peripheral Maria Undarum and Spumans deposits around the Crisium basin provide important records of small-scale volcanic evolution along the outer-ring regions of large impact basins during the early history of the Moon. Their ages constrain the timing and duration of basalt emplacement beyond major impact basins. These mare deposits therefore complement the studies of large basin maria and improve our understanding of the spatial and temporal evolution of lunar volcanism.

2. Datasets and methodology

2.1. Basalt unit definition and composition analysis

We referred to the global lunar mare extent mapping of Nelson et al. (2014), available through the LROC GIS data archive, for the initial identification of mare units in the study region. Nelson et al. (2014) manually delineated mare boundaries in ArcGIS at cartographic scales up to 1:20,000 by integrating geomorphological characteristics and

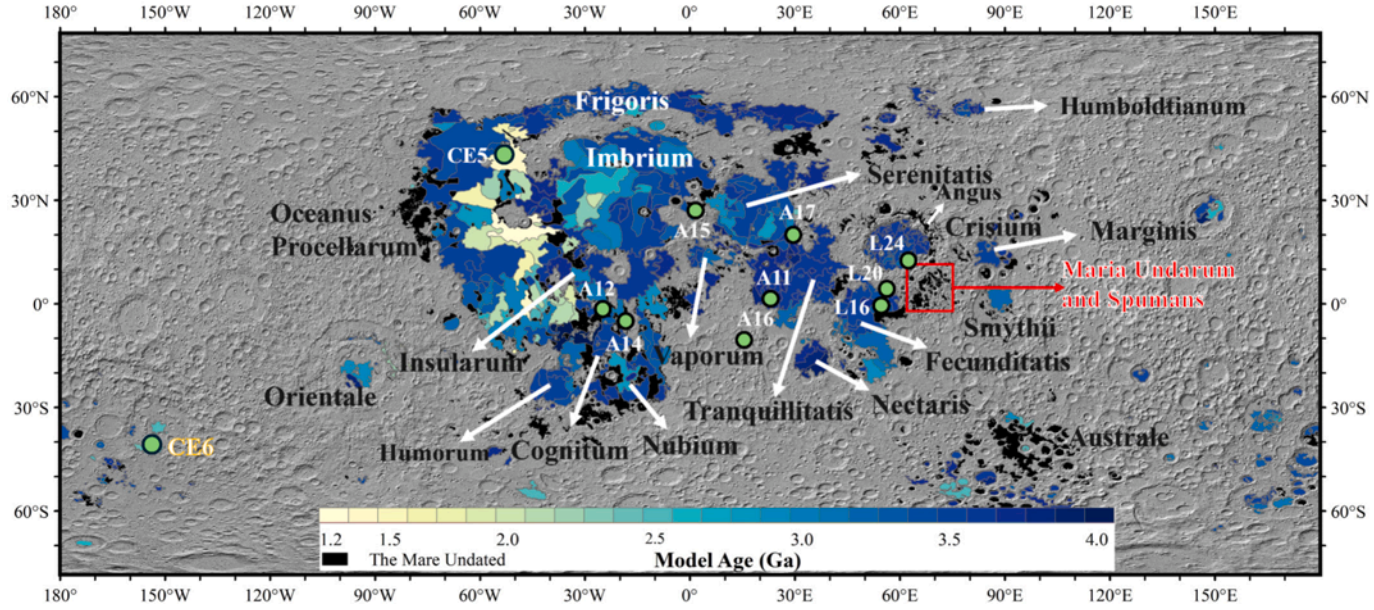


Fig. 1. Distribution of dated and undated mare units on the global Moon. The reported absolute model ages of the dated units (n = ~500) are compiled from various previous studies (Hiesinger et al., 2006, 2011a, 2011b; Morota et al., 2009; Whitten et al., 2011; Cho et al., 2012; Haruyama et al., 2009; Morota et al., 2011; Trieloff et al., 1998; Pasckert et al., 2015, 2018; Jin et al., 2025). The black-filled areas represent the undated regions and green circles denote the positions of individual landing sites. The basemap is a hillshade of Lunar Orbiter Laser Altimeter 256 pixels/degree topography (Smith et al., 2010). All maps in this study are presented in a simple cylindrical projection with a central meridian of 0°. North is toward the top unless otherwise specified. (For interpretation of the references to colour in this figure legend, the reader is referred to the web version of this article.)

spectral differences between mare basalts and surrounding highland materials, using multiple remote-sensing datasets, including LROC WAC mosaics (100 m/pixel) and Clementine UVVIS spectral products. Based on the Kaguya Multiband Imager (MI) data (20 m/pixel), we applied the classical band-ratio pseudocolor composite method following Lucey et al. (2000), in which the ratios of 750 nm/415 nm, 750 nm/950 nm, and 415 nm/750 nm were assigned to the red, green, and blue channels, respectively, in combination with the FeO and TiO_2 abundance imagery to subdivide the mare basalts into individual basalt units. The delineation was based on integrated variations in multispectral reflectance and elemental abundances among different basaltic units, reflecting their distinct compositional characteristics. In the band ratio composite, the lunar highlands are depicted in shades of red, yellow-orange units denote iron-rich, low-titanium basalts, blue hues indicate iron-rich, high-titanium basalts, and pale cyan/green tones represent low-iron, low-titanium basaltic materials (Fig. 3a). On the basis of the definition of mare basalt units, it is feasible to conduct CSFD measurements and age calculations for each unit.

We calculated FeO and TiO_2 abundances from Kaguya MI reflectance data. The abundance of FeO was calculated using the algorithms of Lemelin et al. (2015):

$$\theta_{Fe1} = -\arctan[(R_{950}/R_{750}-1.39)]/(R_{750}-0.04) \quad (1)$$

$$\theta_{Fe2} = 0.065^{*}\exp^{(3.6681^{*}\theta Fe1)} \quad (2)$$

$$FeO\ (\mathrm{wt\%}) = (1.0708^{*}\theta_{Fe2}) - 0.39863 \quad (3)$$

The abundance of TiO_2 was derived employing the algorithms developed by Otake et al. (2012):

$$\theta_{Ti} = \arctan\{[(R_{415}/R_{750}) - 0.208]/R_{750} - (0.108))\} \quad (4)$$

$$TiO_2\ (\mathrm{wt\%}) = 0.72^{*}\theta_{Ti}{}^{14.964} \quad (5)$$

where, R_{xxx} means reflectance at certain wavelength in nanometer. The uncertainties of the Kaguya MI-derived FeO and TiO_2 abundances are approximately 1 wt.% and 0.43 wt. %, respectively, relative to compositions of returned lunar sample measurements (Lemelin et al., 2015; Otake et al., 2012). Statistical analyses of the derived elemental abundances were conducted for each basalt unit to quantify inter-unit compositional variations. Additionally, the lunar surface mineral abundance maps derived from Kaguya MI data (59 m/pixel; Lemelin et al., 2016; Lemelin et al., 2019) were used to investigate mineralogical variations within the studied mare region. The Kaguya MI-derived mineral abundances are subject to uncertainties related to spectral unmixing, photometric effects, space weathering, and sub-pixel mixing (Lemelin et al., 2016; Lemelin et al., 2019; Shi et al., 2026). Lemelin et al. (2015) estimated an uncertainty of approximately 8 wt. % relative to measurements of returned lunar samples for the MI-derived mineral abundances.

2.2. Absolute model age determination

The CSFD measurement is a well-established and powerful remote-sensing technique for deriving the absolute model ages of unsampled planetary surfaces. In short, in order to derive the age of a basalt unit, two procedures must be implemented: (1) accurately measuring the crater count working area in each unit and (2) accurately measuring the diameter of each primary impact crater larger than the completeness diameter in the working area (Hiesinger et al., 2000). The completeness diameter is the estimated minimum crater diameter above which the crater inventory is considered complete within the counting area (Robbins et al., 2018). Therefore, based on the high-resolution Kaguya Terrain Camera (TC) imagery data (10 m/pixel; Haruyama et al., 2008), we utilized the CraterTools (Kneissl et al., 2011) implemented in ArcMap to measure the diameters of impact craters within the defined mare units. Additionally, although CraterTools uses a sinusoidal projection for crater measurements, the areas of the counting units depend on the projection of the ArcMap working environment, which was simple cylindrical in this study. Therefore, we used the equal-area Mollweide projection to calculate the surface areas of individual basalt units.

To minimize the effect of secondary craters on the accuracy of ages (McEwen and Bierhaus, 2006), we have implemented the following steps to address this issue: (1) Areas clearly affected by secondary craters (e.g., crater clusters/chains) were excluded from the crater count working area. (2) The minimum counting crater diameter was selected based on the balance between crater population statistical reliability (more is better) and the workload of crater measurements. A larger minimum crater diameter for age fitting of 700 m was adopted for large mare units with sufficient crater populations to reduce uncertainties from degraded small craters, incomplete detection, and potential secondary crater contamination. For smaller mare units, a lower minimum counting crater diameter of 200 m was used to obtain sufficient crater statistics. The effect of diameter for age fitting selection was further evaluated using the Con unit as an example, where the 700 m diameter provided a better fit to the lunar production function than the 200 m case (Fig. S1; Xiao and Strom, 2012). We assessed crater-count completeness in the U2 mare unit as a representative case study to illustrate the selection of the minimum diameter for age fitting (Fig. S3). The crater dataset includes craters with diameters ≥200 m, extending below the 500 m manual-counting threshold. The $\sqrt{2}$-binned incremental distribution yields an estimated completeness limit of approximately 354 m, based on the lower boundary of the bin immediately larger than the most populated bin (Robbins and Hynek, 2012; Fig. S3a). Gaussian kernel density estimation (Robbins et al., 2018), combined with the derivative-based slope-recovery criterion, gives an estimate of approximately 400 m (Fig. S3b). Both estimates are below the manual-counting threshold. We retained a more conservative minimum diameter of 700 m for age fitting to reduce potential effects of incompleteness and uncertainties in small-crater identification and measurement. The differential distribution and fits over different diameter ranges provide further context for the choice of manual-counting diameter threshold (Fig. S3c). Although these estimates are specific to the U2 unit, the same selection principle can guide assessments of other units, accounting for their counting conditions, crater populations, and suitable fitting ranges. (3) Within the selected counting areas, individual potential secondary craters were identified and excluded based on their morphological characteristics, including irregular shapes, clustering patterns, and crater chains (McEwen and Bierhaus, 2006). We utilized the specialized crater population analysis software CraterStats (Michael and Neukum, 2010), and the lunar production and chronology functions to perform age fitting from the measured crater population. The lunar production function is presented by an eleventh-degree polynomial:

$$\log(N_{cum}) = a_0 + \sum_{j=1}^{11} a_j(\log(D))^j \quad (6)$$

where N_{cum} is the cumulative number of craters per km^2 per Ga (billion years), a_0 represents the amount of time over which a certain unit has been exposed to meteoroid bombardment, and D is the crater diameter in km (Neukum, 1983; Neukum and Ivanov, 1994; Neukum et al., 2001). The parameters a_0 to a_{11} are assigned well-established values (Neukum et al., 2001). The empirically derived lunar chronology function of Neukum et al. (2001) is expressed by the following equation:

$$N_{cum}\ (D \geq 1\ \mathrm{km}) = 5.44 \times 10^{-14}[\exp(6.93 \times t) - 1] + 8.38 \times 10^{-4}\ t \quad (7)$$

In this equation, t is the crater accumulation time (crater retention age) in Ga, and N_{cum} ($D \geq 1$ km) is the cumulative density of craters ≥1 km in diameter.

However, CSFD-derived AMAs are affected by uncertainties related to crater identification, limited crater statistics, secondary crater contamination, crater degradation, saturation effects, and subsequent

resurfacing. In addition, variations in target properties and subsurface structures may introduce further uncertainties into crater scaling. Therefore, careful crater identification and measurement, conservative minimum counting crater diameter thresholds, and appropriate statistical fitting approaches are required to improve the reliability of CSFD age estimates. In this study, we adopted the Poisson probability approach of Michael et al. (2016) for CSFD age determination, which avoids cumulative effects and binning dependence. Differential CSFDs were used to evaluate crater population distributions and deviations from the production function.

2.3. Mare thickness estimation

Upon meteoroids impacting the lunar surface, subsurface materials are excavated and exposed within the resultant craters and their ejecta blankets. A lunar mare unit is filled by basaltic deposits with a finite thickness. When impact craters penetrate the mare layer, they excavate the underlying feldspathic material, creating a distinct compositional contrast with the overlying basaltic component. To determine the excavation depth of the studied craters, we used the equation proposed by Melosh (1989), which describes the relationship between the diameter and maximum excavation depth:

$$H_{exc} = 0.1 \times D_t \quad (8)$$

$$D_t = 0.84 \times D \quad (9)$$

where H_{exc} represents the excavation depth, D_t is the transient crater diameter, and D is the rim-to-rim diameter. The lower and upper bounds of the basalt thickness are determined by the excavation depths of the largest crater that does not penetrate the basalt layer and the smallest crater that penetrates, respectively.

We referred to the FeO and plagioclase abundance maps to determine whether a crater had penetrated the surface basalt layers (Fig. 4). We used the excavation depth of the largest unpenetrated crater as the lower limit of the mare thickness and the smallest penetrated crater as the upper limit. However, in most small mare units within the study area, penetrated craters are not clearly observed. Therefore, for most studied maria, we can only constrain the lower limit of the mare thickness. Given that space weathering effects and exogenous ejecta can influence the spectral characteristics of impact craters, we selected superposed craters within each mare unit that have high albedo, high optical maturity (immature), and well-defined edges. We also endeavored to select as many craters as possible to enhance the precision of basalt thickness estimation. From the surface area and thickness values, we also calculated the volume of basalt in each mare unit.

However, several assumptions and limitations should be considered. The Melosh (1989) scaling relationship provides an estimate of crater excavation depth based on simplified crater scaling models and does not explicitly account for variations in target properties, crater morphology, and complex subsurface structures. Its applicability may therefore vary with crater size and target conditions, particularly for craters near the transition from simple to complex morphology. In addition, mare basalts are not necessarily homogeneous layers but may consist of multiple flows, buried basin ejecta, and heterogeneous crustal structures, which may produce spatial variations in the basalt–substrate interface and introduce uncertainties into thickness estimates. Alternative approaches, such as CSFD curve shape analyses (Hiesinger et al., 2002), have also been applied to estimate mare basalt thickness. However, in this study, no clear breaks or resurfacing signatures were identified in the CSFD curves. Therefore, the derived values should be interpreted as estimates of the exposed mare basalt unit thickness rather than the total thickness of the subsurface basalt sequence. Future constraints from geophysical datasets, such as gravity measurements, may further improve estimates of subsurface structures.

3. Geological context and characteristics of Maria Undarum and Spumans

Basalt deposits of the Maria Undarum and Spumans are mainly distributed between the inner (505 km diameter) and outer main (1076 km) rings (Neumann et al., 2015) of the Crisium basin (Fig. 5) and span a longitudinal range of 58° to 82°E and a latitudinal range of 5°S to 20°N. This region is encircled by four major lunar maria, Mare Crisium

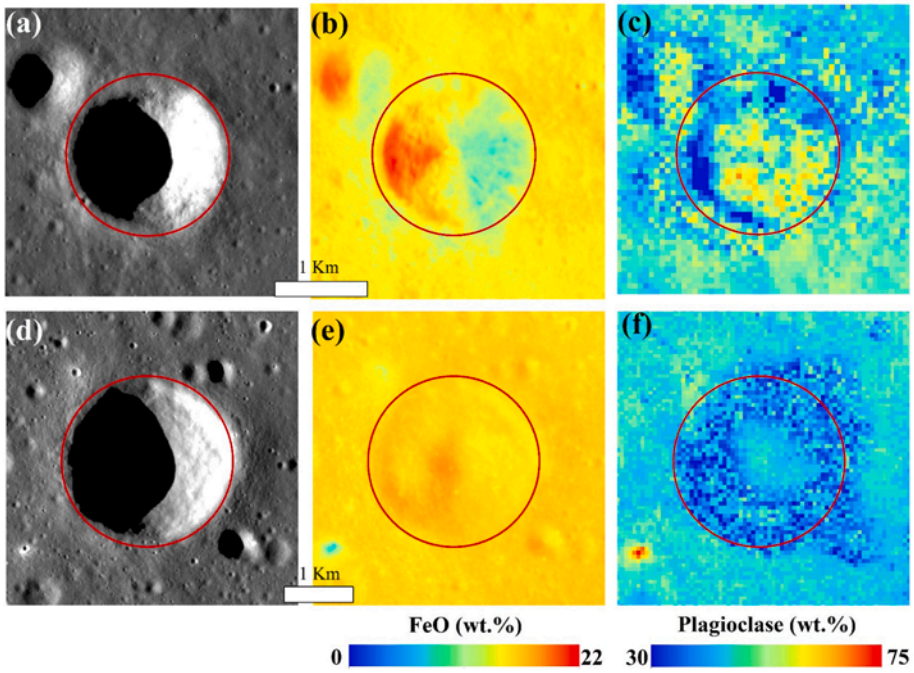


Fig. 4. Panels of (a–c) a representative large un-penetrated crater (centered at 8.24°N, 69.12°E, 1.75 km diameter) and (d–f) a small penetrated crater (centered at 6.1°N, 79.6°E, 2.46 km diameter) in the U3 mare unit: (a, d) Kaguya TC image (Haruyama et al., 2008), (b, e) Kaguya MI FeO abundance (Lemelin et al., 2015), and (c, f) plagioclase abundance (Lemelin et al., 2016, 2019).

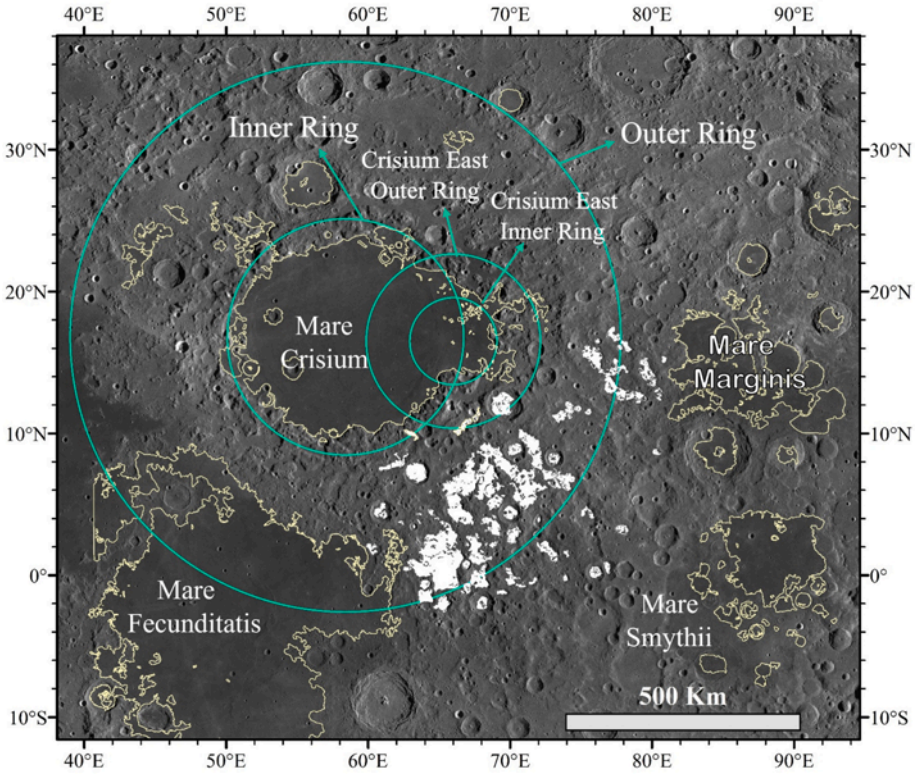


Fig. 5. Regional context of Maria Undarum and Spumans. The base map is cropped from the LROC-WAC image mosaic (100 m/pixel). The study area delineated is highlighted in solid white, while the four surrounding major lunar maria are demarcated by yellow outlines. Both the inner and outer rings of the Crisium basin, as well as those of the eastern Crisium basin (Neumann et al., 2015), are depicted as turquoise circles. (For interpretation of the references to colour in this figure legend, the reader is referred to the web version of this article.)

to the northwest, Mare Fecunditatis to the west, Mare Marginis to the northeast, and Mare Smythii to the southeast (Fig. 2). Compared to the small mare patches within Maria Undarum and Spumans, the surrounding four maria are characterized with much more extensive mare filling (Fig. 5). Specifically, Mare Fecunditatis is characterized by thin, multi-stage low-to-moderate titanium lavas (Rajmon and Spudis, 2000; Zhao et al., 2022); Mare Marginis is notable for magnetic anomalies within the nearside/farside transition zone and high-titanium basalt units (Garrick-Bethell et al., 2011; Gillis and Spudis, 2000); Mare Smythii displays complex late-stage magmatic-tectonic activity and widespread floor-fractured craters (Wichman and Schultz, 1995). The Crisium basin formed during the Late Nectarian period (~3.9–4.1 Ga; Wilhelms, 1987; Stöffler and Ryder, 2001; Orgel et al., 2018), and the surrounding mare basalts were emplaced afterward during the Imbrian to Eratosthenian periods. Maria Fecunditatis, Marginis, and Smythii have estimated ages of ~3.8–3.6 Ga, ~3.8–3.4 Ga, and ~ 3.5–3.2 Ga, respectively (Hiesinger et al., 2011a; Gillis and Spudis, 2000; Wichman and Schultz, 1995). Therefore, these maria represent post-Crisium volcanic activity. The Crisium impact likely has modified the regional crustal structure and provided favorable conditions for subsequent basaltic volcanism by creating accommodation space and facilitating magma ascent, although the post-basin mare basalts were not directly produced by the impact event itself.

The Crisium basin is a typical multi-ring impact basin, with massive lava filling, located in the northeastern region of the lunar nearside. The basin exhibits several concentric structural features, including prominent inner and outer rings, which formed during the transient excavation, collapse, and gravitational modification of the crust following the large-scale impact event. The Crisium impact event not only formed the basin structure but also caused extensive modification of the surrounding crust through ejecta emplacement, concentric deformation, and the formation of local depressions in the basin exterior. These impact-related structures may have provided favorable sites for later basalt emplacement; however, the distribution of surrounding mare units was also influenced by regional crustal properties and subsequent magmatic processes (Head III et al., 1978; Spudis et al., 1989). Mare Crisium, emplaced mainly within the inner ring of the Crisium basin, is bounded by Mare Marginis to the east and Mare Tranquillitatis to the west. Mare Crisium has a roughly circular outline and relatively flat surface topography. The average slope of the mare surface is less than 1°, though it is dotted with numerous small wrinkle ridges and rilles. The mare is encircled by highland massifs, which are the remnants of the original impact basin and several kilometers higher than the mare plains. Abundant impact craters of various sizes are distributed across both the interior and margins of the mare plain. These craters provide critical clues for investigating the regional impact and geological history. Based on compositional variations, Head III et al. (1978) classified the basalts within the Crisium basin into three distinct types: Fe-rich and Mg-rich Ti-bearing basalts, very-low-titanium (VLT) and low-titanium (LT) basalts, indicating diverse mantle sources and magma evolution processes. Combined with the broad range of model ages (~2.4–3.7 Ga) derived from CSFD measurements (Hiesinger et al., 2011b; Lu et al., 2021), these compositional variations suggest that Mare Crisium experienced prolonged and episodic volcanic activity after basin formation. The early emplacement of Ti-rich basalts likely reflects the initial stage of mantle melting and magma ascent following crustal modification, whereas younger LT and VLT basalts indicate continued volcanic activity involving progressively different mantle sources and melting conditions. Therefore, the chronology and compositional diversity of Mare Crisium basalts provide important constraints on the duration and evolution of post-basin volcanism. Because Maria Undarum and Spumans are located between the inner and outer rings of the Crisium basin, their ages and compositions provide an opportunity to assess whether basin peripheral mare deposits were genetically related to the long-term

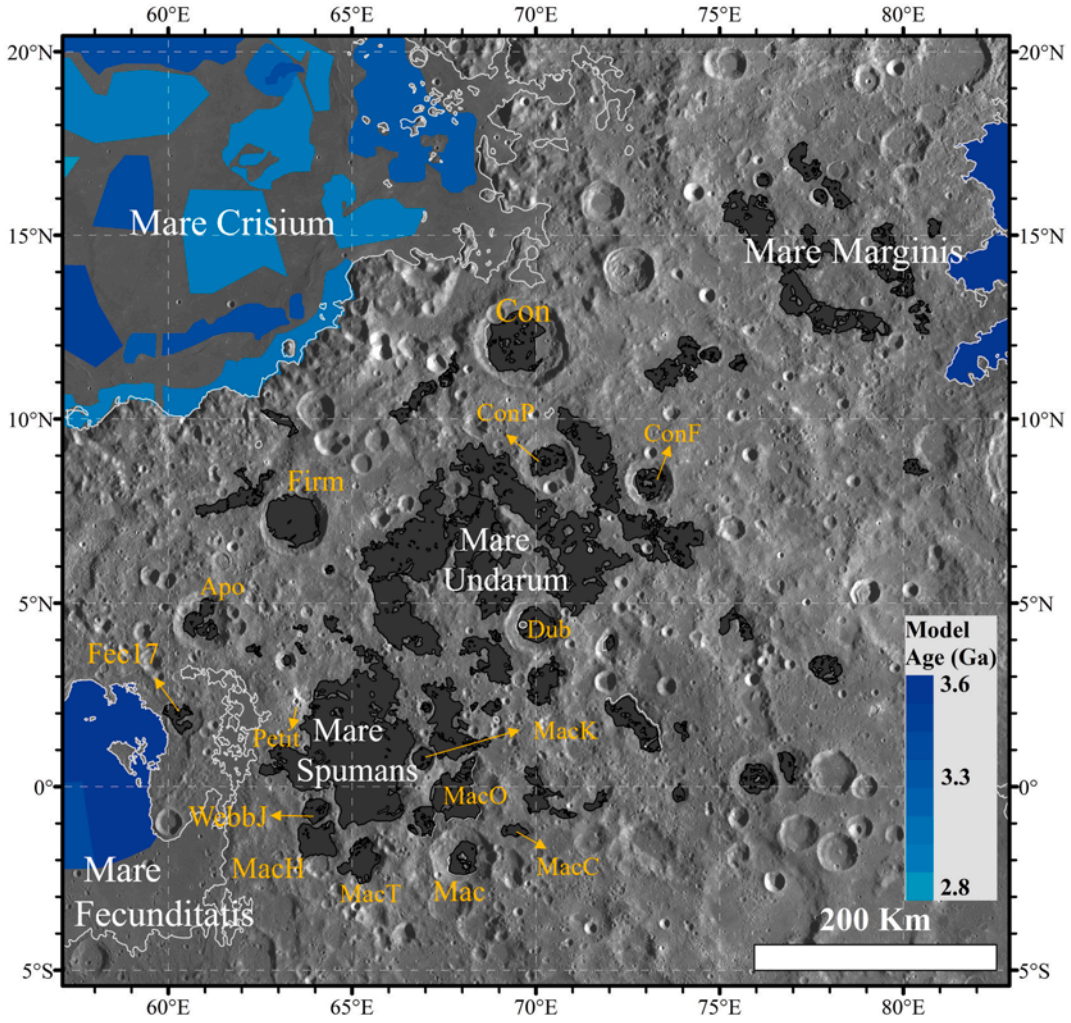


Fig. 2. Lunar Reconnaissance Orbiter Wide-Angle Camera (LROC-WAC) image mosaic (100 m/pixel) of the study area (Speyerer et al., 2011). The dark-filled areas represent the mare units within the study region. The areas delineated by white boundaries denote the surrounding lunar maria, with colour-filled areas representing the dated sub-regions therein. The orange abbreviations indicate representative impact craters within the study area (Con is short for Condorcet, Mac for Maclaurin, Apo, Dub, Firm for Apollonius, Dubyago, and Firmicus craters, respectively).

volcanic evolution of the basin or represent independent regional magmatic activity. Constraining these characteristics is therefore essential for understanding the spatial and temporal evolution of volcanism associated with the Crisium basin.

On the basis of the elevation map and the topographical profiles (Fig. 6), it is evident that, in contrast to the surrounding four maria, mare patches in Maria Undarum and Spumans regions exhibit relatively higher elevations. Elevations across these maria span −3971 m to 638 m, with an average elevation of −1400 m. Mare Undarum is situated in the transition zone between the Crisium basin interior and exterior highlands, and has very irregular zonal outlines. Topographically, its elevation (mean value −727 m) is relatively higher than that of Mare Spumans (−1713 m mean elevation). Its elevation is approximately 1–2 km lower than that of the surrounding highlands. The western region of Mare Undarum is relatively flat compared with the eastern region, which is surrounded by several large impact craters (Condorcet and Dubyago). Mare Spumans is situated along the northern margin of Mare Fecunditatis, separated from the latter only by a discontinuous highland belt ~10 km in width. It is also composed of many small mare patches. The largest patch has a broadly elliptic outline and some small patches are spatially connected with Mare Fecunditatis to the west. These landforms are interpreted to represent small-scale volcanic structural complexes, likely attributed to the contraction of shallow magma chambers or associated volcanic-tectonic deformation (Bennett et al., 2016).

It is inferred that these two maria were emplaced on the continuous ejecta deposits of the Crisium basin which formed during a period of high cratering flux, dated to ~3.9–4.1 Ga (Baldwin, 1974; Nunes et al., 1974; Schaeffer and Husain, 1974; Orgel et al., 2018). The cratering sequence in the Maria Undarum and Spumans region can be categorized into three distinct stages: Stage I craters, which formed during a period of high impact flux, are highly degraded and covered by ejecta from the Crisium basin; Stage II craters formed on the surface that had already been mantled by ejecta and were subsequently flooded by mare basalts; Stage III craters formed after emplacement of mare basalts, during a period characterized by a much lower and more constant impact rate (De Hon, 1975a, De Hon, 1975b; Neukum et al., 2001; Lena et al., 2008). This classification provides a temporal framework for separating pre-mare and post-mare crater populations. In particular, Stage III craters are the primary population used for CSFD-based AMA determination because they formed after mare emplacement and directly record the impact history of the basalt surface. In contrast, the distribution and burial characteristics of Stage I and Stage II craters provide important constraints on the pre-mare surface and the subsequent flooding process by mare basalts, which are essential for reconstructing the volcanic evolution and estimating basalt thickness. However, previous studies of

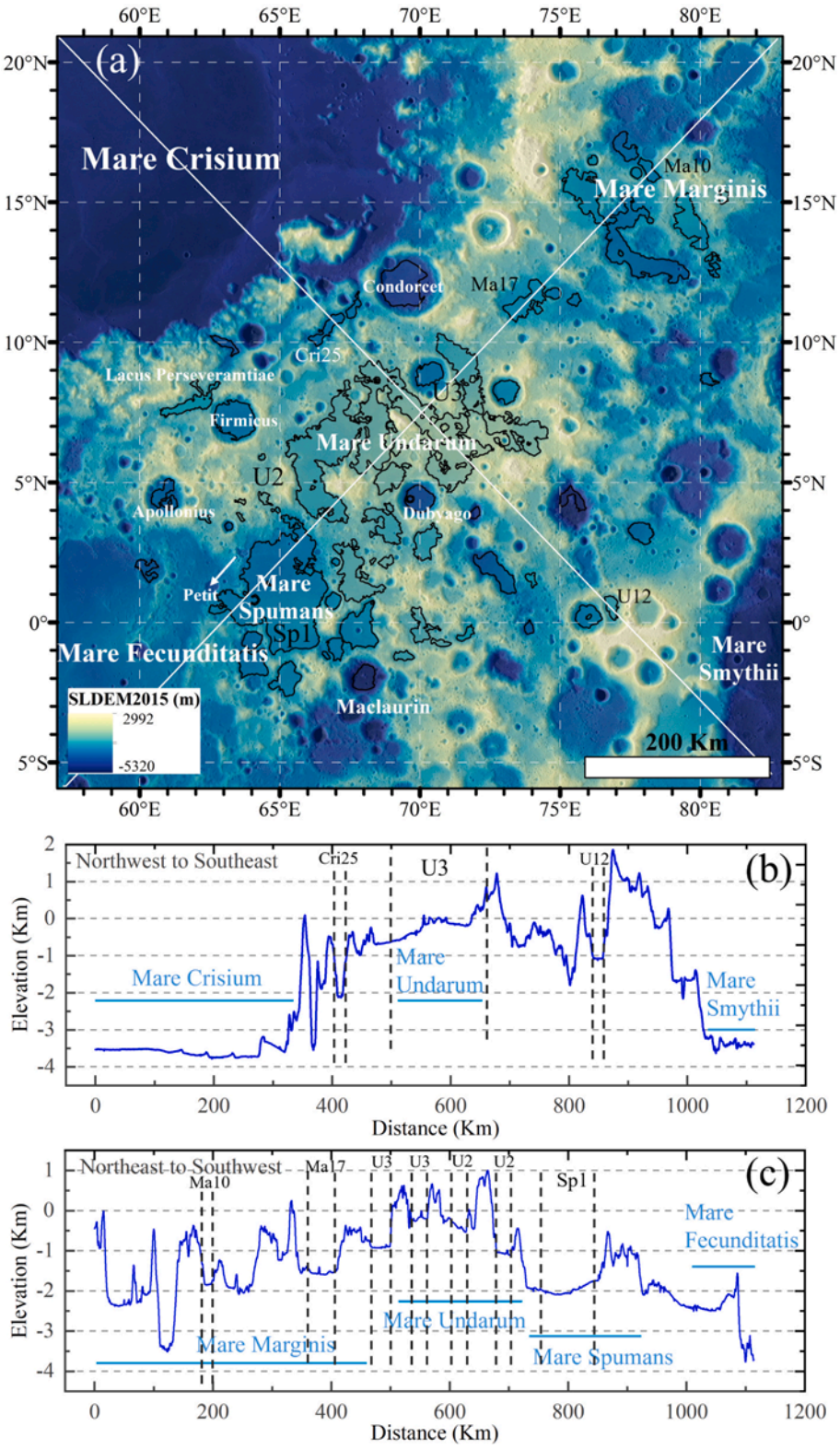


Fig. 6. (a) SLDEM2015 (512 pixels/degree) topography (Barker et al., 2016) overlain on Kaguya TC image of the study area. Black polygons indicate mare basalt units. (b) a northwest-southeast and (c) a northeast-southwest topographical profile across the study area derived from SLDEM2015.

this region lacked precise chronological investigations of these two maria, limiting our understanding of regional volcanic activity evolution. Moreover, the orbital geochemistry datasets revealed spatial compositional variations within the Maria Undarum and Spumans region, particularly in FeO, MgO, and Al abundances, reflecting variable contributions from mare basalt and surrounding highland materials (Clark and Hawke, 1987). Building on these findings, we suggest that the Maria Undarum and Spumans are ideal for constraining the chronology, composition, and evolution of small-scale mare volcanism on the Moon.

4. Results

4.1. Mare unit definition

The Maria Spumans and Undarum, and surrounding small maria are composed of many small mare patches (Figs. 1 and 2). Based on spectral variations across individual basalt units, we defined 66 previously undated mare units: 16 in Mare Undarum, 18 in Mare Spumans, 14 in Mare Marginis, 3 in Mare Crisium, 6 in the Maclaurin and its satellite (Maclaurin C, H, K, O, T) craters, 3 in Condorcet and its satellite (Condorcet P, F) craters and one each in Mare Fecunditatis, Lacus Perseverantiae, and craters Webb J, Apollonius, Dubyago, and Firmicus (Fig. 2). Building upon the global lunar mare boundary map compiled by Nelson et al. (2014) and the nomenclatural method of previous chronological studies (Hiesinger et al., 2006, 2011a, 2011b), we named all delineated basalt units using abbreviations of their host mare or impact craters (names already used in previous studies have been avoided): Sp1–Sp18 for mare units in Mare Spumans, U1–U16 for Mare Undarum, Ma5–Ma18 for southwest Mare Marginis (Ma1–Ma4 are already in Hiesinger et al. (2011a)), Cri24–Cri26 for southeast Mare Crisium (23 mare units have been defined and dated previously (Hiesinger et al., 2011b)), Con, ConP, ConF for Condorcet and adjacent craters floor maria, Mac, MacC, MacH, MacK, MacO, MacT for Maclaurin and adjacent craters floor maria, Fec17 for Mare Fecunditatis (F1–F16 were already in Hiesinger et al. (2006)), LP for Lacus Perseverantiae, and Apo, Dub, Firm for the floor maria of Apollonius, Dubyago, and Firmicus

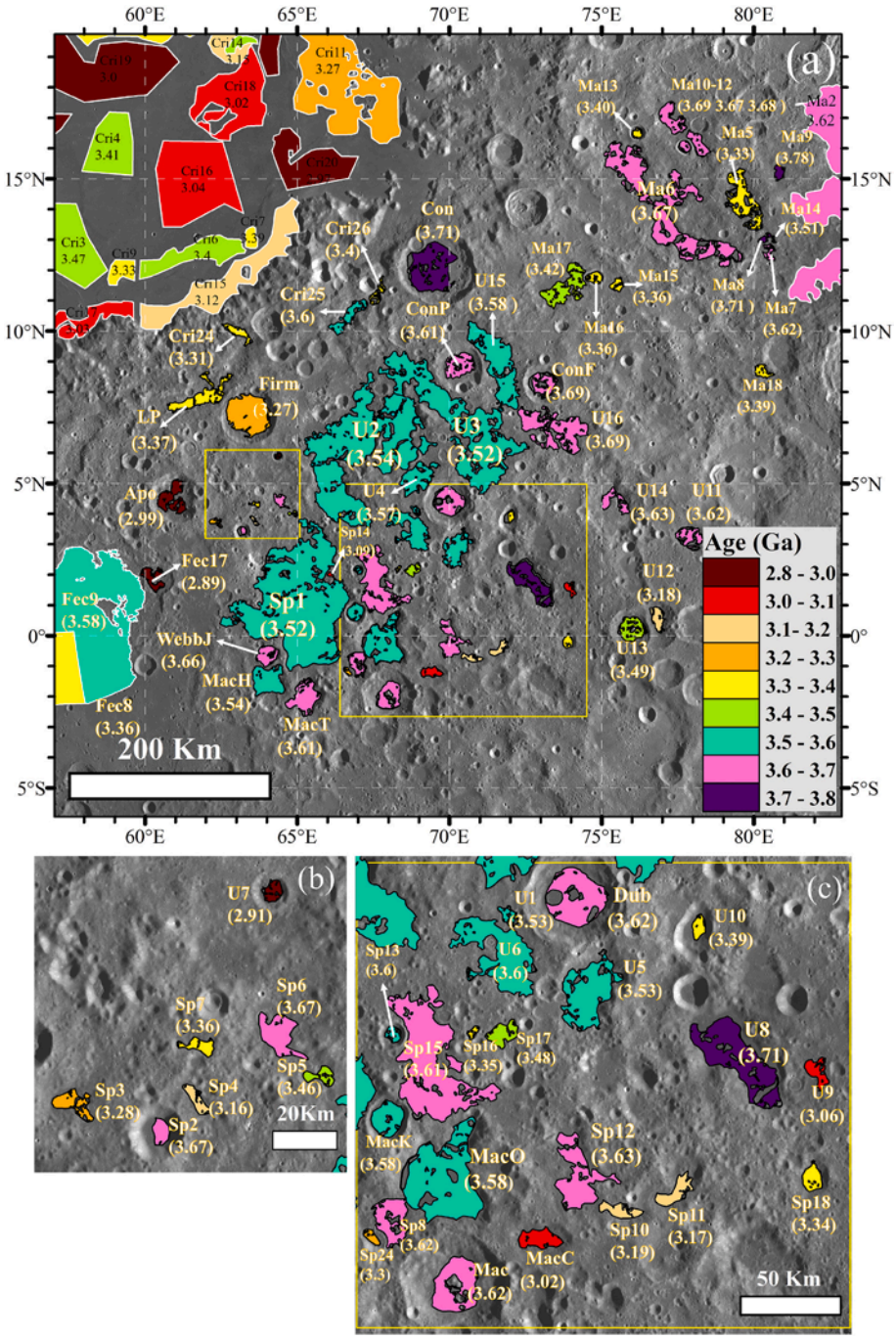


Fig. 7. (a) Colour-coded map of the absolute model ages for mare basalts in our study area with the LROC WAC mosaic as a base map. All age values are given in Ga. (b) and (c) Enlarged views of the northern and eastern parts of the Sp1 unit, respectively. The white outlined polygons delineate the surrounding mare basaltic units.

craters, respectively.

The 66 mare basalt units have a total surface area of ~48,600 km^2, and exhibit a leptokurtic areal distribution pattern. The leptokurtic distribution indicates that most basalt units are concentrated within a narrow range of small surface areas, whereas a few large mare units contribute to the extended tails of the distribution. This uneven distribution is reflected by the difference between the mean area (736 km^2) and median area (250 km^2). Spatially, larger units occur mainly in the central region, with smaller units distributed toward the margins. Three large (~5,000–9,000 km^2) mare units (Sp1, U2, and U3) are defined in the main body of Maria Spumans and Undarum (Fig. 7), with a total surface area of ~21,000 km^2, nearly half (43%) of all the 66 mare units. The 18 distinct basalt units in Mare Spumans region cover an overall area of approximately 12,000 km^2. The main unit (Sp1) is encircled by surrounding smaller basalt units, with an area of about 8,800 km^2, accounting for roughly 75% of all Mare Spumans units. To the east of Sp1 lie two relatively large basalt units (MacO and Sp15), with a combined area of 2,568 km^2. To the south of Sp1, three relatively large crater floor maria (MacT, MacH, and WebbJ) collectively cover a total area of 1,624 km^2. Smaller basalt units within the Mare Spumans region occur

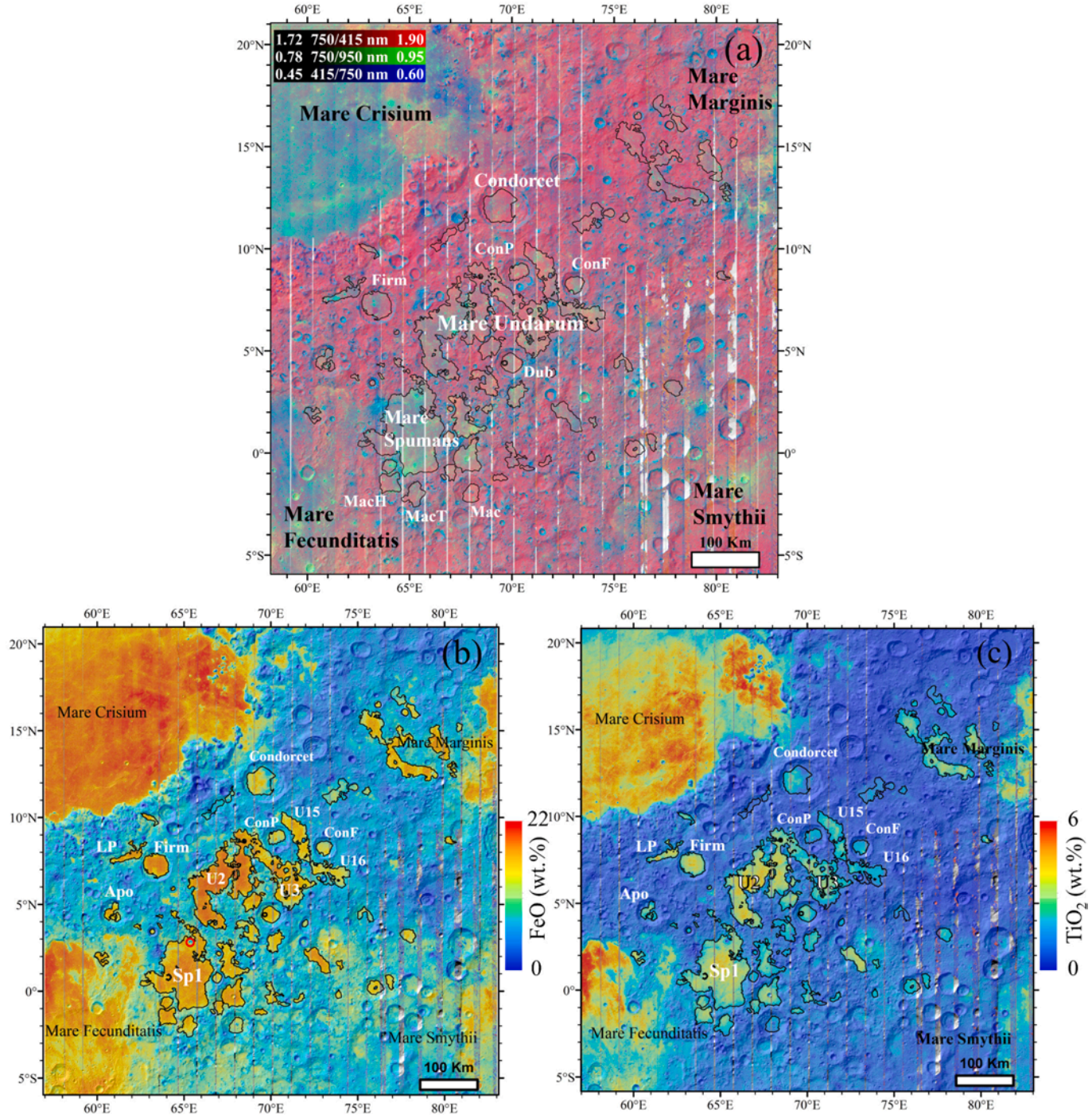


Fig. 3. (a) Band ratio composite (750 nm/415 nm in red, 750 nm/950 nm in green, 415 nm/750 nm in blue), (b) FeO content (the area enclosed by the red circle denotes a large impact crater with compositional anomalies), and (c) TiO_2 content maps of Maria Undarum, Spumans, and surrounding regions derived from the Kaguya MI data. (For interpretation of the references to colour in this figure legend, the reader is referred to the web version of this article.)

predominantly in the northwest and southeast of Sp1 (Fig. 7). The main units of Mare Undarum are U2 and U3, which together cover an area of approximately 12,245 km^2 and constitute around 63% of all Mare Undarum units. Although the two units are spatially connected, their compositional signatures differ markedly (Fig. 3b, 3c). U2 has higher mean TiO_2 and FeO abundances (3.4 wt. % and 15.9 wt. %, respectively) compared with U3 (2.7 wt. % and 14.2 wt. %, respectively), indicating distinct compositional characteristics between the two units. To the east of U3, there are two relatively large, irregular mare basalt units (U15 and U16), which collectively cover an area of 3,041 km^2 and account for approximately 16% of all Mare Undarum units. A cluster of small mare patches (U9−U14, 1347 km^2 in total) is distributed in the southern and eastern margin of Mare Undarum. In addition, several mare-filled impact craters are located in the vicinity of Mare Undarum: the Firmicus crater, with a diameter of ~45 km and an area of 1,332 km^2 floor mare (Firm) lies in the northwest; the ~50 km diameter Condorcet crater, with floor filled with 1,471 km^2 mare (Con), lies to the north; and the ~37 km diameter Dubyago crater with the floor mare area of 521 km^2 (Dub), is positioned north of the U3 unit. Mare Marginis basalt units (Ma5–Ma18, ~6,380 km^2) are located in the northeast of Mare Undarum and are characterized by irregular, sinuous belt-like outlines. On the southeast flank of the Crisium basin, several small chain-shaped basalt units (Cri24–Cri26) collectively cover a total area of ~665 km^2.

Following the derivation of AMAs for the 66 basalt units, we evaluated whether adjacent basalt patches may represent a single geological unit by comparing their ages and compositional characteristics (FeO and TiO_2 abundances). Although some patches are spatially adjacent, their chronological and compositional characteristics do not show similarities that would justify merging them into larger units. Therefore, we retained the original classification of individual basalt units. This approach avoids combining spatially adjacent but potentially unrelated basalt deposits and preserves the observed variations in their volcanic histories.

4.2. AMAs of the mare basalts

We compiled the central coordinates, surface area, counted crater number and spatial density, age, and mean TiO_2 and FeO abundances for each mare unit (Table 1). The spatial distribution of impact craters in the four largest basalt units (U2, U3, Sp1, and Ma6) is shown in Fig. 8, with CSFD plots presented in Fig. 9. Secondary craters were excluded prior to analysis (Fig. 8). Given that the four mare units have relatively large surface areas, only impact craters ≥700 m in diameter were retained to ensure statistical validity. The AMA of the U2 unit (~7,240 km^2) was determined based on 151 impact craters with diameters ≥700 m. For U3 unit (5,006 km^2), 98 impact craters were utilized for age fitting. Both U2 and U3 units yielded model ages ~3.5 Ga (3.54 Ga and 3.52 Ga, respectively). In Sp1 unit, 168 impact craters were employed for age fitting, also yielding a model age of 3.52 Ga. Ma6, the largest basalt patch in Mare Marginis (3,290 km^2), hosts 114 impact craters ≥700 m and yields an older modeled age of ~3.67 Ga (Throughout this manuscript, the term "age" refers to AMA) derived from CSFD measurements.

On the basis of CSFD measurements of impact craters, we concluded that the absolute model ages of the 66 basalt units range from ~2.89 to 3.78 Ga. The youngest basalt unit Fec17, a small mare patch located on the northeastern periphery of Mare Fecunditatis, formed during the Eratosthenian period (with a model age of 2.89 Ga). In contrast, most of the investigated basalt units were emplaced during the Imbrian period. The oldest basalt unit, Ma9 in the Mare Marginis region, has an AMA of ~3.78 Ga, representing one of the oldest mare basalt units in this study region. The model age range for the 18 mare units (Sp1–Sp18) in the Mare Spumans region is ~3.09–3.67 Ga. The main part of Mare Spumans region (Sp1) has an age of approximately 3.52 Ga. Additionally, the oldest basalt unit in Mare Spumans, Sp2 in the northwest of Sp1, has a model age of ~3.67 Ga. The ages of the two relatively larger basalt units Sp12 and MacO, as well as Mac, on the southeast of Sp1 are approximately 3.6 Ga. Several smaller basalt units MacC, Sp4, Sp10, Sp11, and Sp14 (with areas <155 km^2) in the southeast periphery portion have similar ages of 3.2–3.3 Ga, relatively younger than the larger maria in the Mare Spumans region. This phenomenon may reflect localized late-stage volcanic activity during the waning phase of lunar magmatism, consistent with the temporal decline in mare basalt emplacement rates (Head and Wilson, 2017).

The 16 mare units (U1–U16) in the Mare Undarum region exhibit model ages from ~2.91 to 3.71 Ga. The major units, U2 and U3, are both dated to be ~3.5 Ga (3.54 Ga and 3.52 Ga). Older basalts (~3.58–3.71 Ga) are found northeast (U11, U14, U15, U16, ConP and ConF mare) and southeast (U8 and Dubyago crater floor mare (Dub)) of U3. In contrast, the Firmicus crater floor mare (Firm), in the west of U2 unit, exhibits a much younger age of ~3.27 Ga which is also the youngest large circular mare basalt among the 66 basalt units. Compared to the Condorcet crater floor mare (Con), dated to be ~3.71 Ga, the Firm unit has a relatively smoother surface and more homogeneous composition as indicated by spectral data (Fig. 3).

4.3. Basalt thicknesses and volumes

The lower limits of the basalt thickness of 16 mare units in the Mare Undarum region range from 47 to 207 m, and the calculated total basalt volume is at least ~3,000 km^3. In the U2 unit, superposed impact crater analysis yields a basalt thickness of 141–248 m, constrained by the largest unpenetrated crater (1.7 km diameter) and the smallest penetrated crater (3.0 km). For the U3 unit, the estimated mare thickness is 207–270 m, based on the largest unpenetrated (~2.5 km) and the smallest penetrated (3.2 km) superposed craters. Using the lower thickness limits and areal extent, the estimated total basalt volume in the U2 and U3 units is at least 2,060 km^3, representing approximately 70% of the total mare fill in the Mare Undarum region. Most basalt units within the Mare Undarum region exceed 100 m in thickness, with only a few peripheral units being significantly thinner (e.g., U1, U7, U9, and U10 < 70 m). Additionally, the thicker mare units are identified on the east (U15, with 137 m as lower limit and 144 m as upper limit; U16, with 148 m as lower limit and 193 m as upper limit) and southeast (U8, 167 m as lower limit) of U3 unit.

The 18 basalt units (Sp1–Sp18) in Mare Spumans exhibit mare thickness lower limits ranging from 41 to 188 m, yielding a total basalt volume of at least 2,000 km^3 for this region. Sp1 unit, the largest and thickest basaltic unit in Mare Spumans, has the largest unpenetrated crater with a diameter of 2.29 km and the smallest penetrated crater of 2.77 km. Accordingly, the basalt thickness of the Sp1 unit is estimated to range from 188 to 227 m. The basaltic volume lower limit of this unit is 1,654 km^3, accounting for ~83% of the total mare volume of Mare Spumans units. On the northwest and southeast of Sp1, 10 small mare units (Sp2–Sp5, Sp7, Sp9, Sp11, Sp14, Sp16 and Sp18) exhibit basalt thicknesses below 70 m. The thinnest units are Sp5 and Sp7 units in the northwest of Sp1, with mean thicknesses of approximately 42 m. Mare basalts in these small mare units are relatively thinner than those in large mare units. This demonstrates that large mare units are formed by much larger volume eruptions.

The minimum thicknesses of the 14 basalt units (Ma5–Ma18) in the Mare Marginis region range from 47 to 148 m, with an estimated total volume of approximately 840 km^3. Except for a few smaller and irregularly shaped basalt units with thicknesses less than 70 m (Ma13, Ma14, and Ma18), the thicknesses of the remaining larger units (Ma5, Ma6, Ma10, Ma11, Ma17) are all greater than 100 m (Fig. 10). The maximum mare thickness occurs in the two largest basalt units in the central portion of Mare Marginis, Ma5 and Ma6, which are approximately 132 m and 148 m, respectively. The minimum basalt thickness is approximately 128 m in Condorcet crater floor mare (Con) and about 110 m in its satellite crater floor maria (ConP and ConF). The average basalt thickness of the floor maria of Maclaurin and its satellite craters is ~128 m. Additionally, the two larger crater floor mare units, Firm and

Table 1
Locations, ages, and compositions of basalt units in this study.

Name	Central Long [°]	Central Lat [°]	Area (km^2)	Age (Ga)	N(1) (10^{-3} km^{-2})	Minimum counting crater diameter (m)	Counted crater number	Crater diameter for age fitting (m)	Crater number for age fitting	Mean TiO_2 (wt%)	Mean FeO (wt %)
U1	68.9°E	4.1°N	44	3.53 + 0.063/−0.094	6.59	300	21	≥300	21	1.7	11.4
U2	67.1°E	6.1°N	7239	3.54 + 0.023/−0.028	5.27	500	541	≥700	149	3.4	15.9
U3	70.3°E	7.0°N	5006	3.52 + 0.031/−0.039	5.28	500	417	≥700	98	2.7	14.2
U4	69.0°E	5.2°N	638	3.57 + 0.036/−0.049	5.16	500	52	≥500	52	2.6	14.3
U5	70.2°E	2.8°N	586	3.53 + 0.047/−0.072	5.13	500	42	≥500	42	2.6	13.2
U6	68.7°E	3.5°N	801	3.60 + 0.029/−0.036	7.00	400	128	≥500	71	2.0	12.6
U7	64.4°E	5.91°N	27	2.91 + 0.30/−0.48	2.98	200	25	≥200	25	2.3	13.8
U8	72.7°E	2.0°N	753	3.71 + 0.025/−0.031	1.04	600	56	≥700	33	3.3	14.3
U9	74.0°E	1.5°N	95	3.06 + 0.25/−0.48	3.34	300	25	≥300	25	2.2	13.7
U10	72.0°E	3.9°N	56	3.39 + 0.11/−0.24	4.27	300	20	≥300	20	1.6	11.3
U11	77.9°E	3.2°N	309	3.62 + 0.042/−0.061	9.22	500	31	≥500	31	3.3	12.6
U12	76.8°E	0.6°N	218	3.18 + 0.21/−0.49	4.02	300	42	≥400	23	2.1	12.9
U13	78.0°E	0.2°N	396	3.49 + 0.072/−0.17	6.48	400	43	≥500	27	2.0	13.3
U14	75.4°E	4.4°N	273	3.63 + 0.042/−0.062	8.33	500	29	≥500	29	1.2	10.6
U15	71.6°E	8.8°N	1592	3.58 + 0.023/−0.027	6.85	400	214	≥600	74	2.1	13.4
U16	73.5°E	6.8°N	1449	3.69 + 0.020/−0.023	1.18	600	98	≥600	98	1.9	12.0
Sp1	65.0°E	1.7°N	8799	3.52 + 0.024/−0.028	5.49	600	321	≥700	168	3.0	15.2
Sp2	63.2°E	3.4°N	33	3.67 + 0.040/−0.057	8.44	300	27	≥300	27	1.8	12.1
Sp3	62.3°E	3.7°N	54	3.28 + 0.099/−0.19	2.91	200	63	≥200	63	1.8	13.0
Sp4	63.6°E	3.8°N	31	3.16 + 0.18/−0.37	2.91	200	35	≥200	35	2.4	12.8
Sp5	64.9°E	4.0°N	30	3.46 + 0.057/−0.096	2.97	200	47	≥200	47	1.8	12.6
Sp6	64.4°E	4.4°N	108	3.67 + 0.037/−0.050	9.67	400	31	≥400	31	2.0	13.1
Sp7	63.6°E	4.3°N	32	3.36 + 0.088/−0.19	4.44	200	43	≥200	43	2.0	12.2
Sp8	67.0°E	0.9°S	249	3.62 + 0.046/−0.072	1.44	500	26	≥500	26	2.5	14.1
Sp9	66.7°E	1.2°S	34	3.24 + 0.14/−0.30	3.16	200	40	≥200	40	1.6	11.9
Sp10	71.7°E	0.4°S	130	3.19 + 0.17/−0.35	2.94	300	38	≥300	38	1.9	12.6
Sp11	70.7°E	0.7°S	99	3.17 + 0.20/−0.43	3.18	300	28	≥300	28	1.4	10.4
Sp12	70.0°E	0.2°S	457	3.63 + 0.032/−0.042	8.07	500	47	≥600	26	2.2	12.5
Sp13	67.0°E	2.2°N	39	3.56 + 0.061/−0.13	5.78	300	20	≥300	20	1.7	12.6
Sp14	66.1°E	2.0°N	21	3.09 + 0.24/−0.49	3.36	200	24	≥200	24	2.1	13.7
Sp15	67.6°E	1.7°N	1456	3.61 + 0.020/−0.023	7.78	500	135	≥600	75	2.3	13.8
Sp16	68.3°E	2.2°N	20	3.35 + 0.12/−0.33	4.41	200	28	≥200	28	1.3	11.4
Sp17	68.8°E	2.2°N	120	3.48 + 0.052/−0.084	4.57	300	49	≥300	49	1.8	11.8
Sp18	73.9°E	0.2°S	97	3.34 + 0.12/−0.30	3.98	300	32	≥300	32	1.9	12.8
Ma5	79.7°E	14.3°N	858	3.33 + 0.10/−0.23	4.4	500	42	≥600	22	3.3	14.6

(*continued on next page*)

Table 1 (*continued*)

Name	Central Long [°]	Central Lat [°]	Area (km^2)	Age (Ga)	N(1) (10^{-3} km^{-2})	Minimum counting crater diameter (m)	Counted crater number	Crater diameter for age fitting (m)	Crater number for age fitting	Mean TiO_2 (wt%)	Mean FeO (wt %)
Ma6	77.1°E	14.1°N	3290	3.67 + 0.019/ −0.022	9.57	700	114	≥700	114	2.3	13.8
Ma7	80.5°E	12.6°N	97	3.62 + 0.048/ −0.060	9.00	400	22	≥400	22	1.9	12.8
Ma8	80.4°E	13.0°N	55	3.71 + 0.043/ −0.050	1.2	300	28	≥400	19	2.3	13.9
Ma9	80.8°E	15.2°N	108	3.78 + 0.035/ −0.048	1.57	500	24	≥500	24	2.1	11.2
Ma10	78.2°E	16.2°N	250	3.69 + 0.034/ −0.045	8.55	500	34	≥500	34	1.7	12.5
Ma11	77.3°E	17.0°N	389	3.67 + 0.029/ −0.037	1.13	500	49	≥600	21	1.3	9.9
Ma12	77.7°E	16.1°N	82	3.68 + 0.041/ −0.059	1.13	400	25	≥400	25	1.8	12.7
Ma13	76.2°E	16.5°N	66	3.40 + 0.11/ −0.32	4.52	300	25	≥300	25	1.8	12.8
Ma14	80.7°E	13.0°N	12	3.51 + 0.068/ −0.11	5.4	200	22	≥200	22	1.6	11.2
Ma15	75.5°E	11.5°N	108	3.36 + 0.099/ −0.24	4.28	300	36	≥300	36	1.3	11.0
Ma16	74.8°E	11.8°N	128	3.36 + 0.090/ −0.20	4.49	300	42	≥300	42	1.1	10.2
Ma17	73.8°E	11.4°N	795	3.42 + 0.046/ −0.066	3.83	400	95	≥400	95	1.4	9.9
Ma18	80.3°E	8.7°N	137	3.39 + 0.078/ −0.16	3.62	300	46	≥300	46	2.1	13.3
Cri24	63.1°E	10.0°N	182	3.31 + 0.095/ −0.20	3.24	300	56	≥300	56	2.1	13.2
Cri25	66.7°E	10.5°N	355	3.60 + 0.043/ −0.063	8.57	400	62	≥600	19	1.0	8.2
Cri26	67.7°E	11.3°N	128	3.40 + 0.11/ −0.26	3.8	300	30	≥300	30	1.2	9.7
Mac	68.0°E	2.0°S	410	3.62 + 0.053/ −0.068	8.57	500	30	≥500	30	1.6	11.5
MacC	69.4°E	1.2°S	153	3.02 + 0.23/ −0.39	3.01	300	37	≥300	37	2.1	14.0
MacH	64.0°E	1.5°S	700	3.54 + 0.039/ −0.055	5.79	500	52	≥500	52	2.8	14.9
MacK	66.9°E	0.8°N	197	3.58 + 0.062/ −0.089	5.95	400	27	≥400	27	2.0	12.8
MacO	67.8°E	0.2°S	1111	3.58 + 0.050/ −0.084	8.51	500	36	≥700	28	2.6	14.9
MacT	65.2°E	2.0°S	635	3.61 + 0.043/ −0.064	7.21	500	47	≥500	47	2.1	13.4
Con	69.4°E	12.1°N	1471	3.71 + 0.024/ −0.029	1.05	600	97	≥700	62	1.9	11.6
ConF	73.1°E	8.3°N	331	3.69 + 0.030/ −0.037	1.93	500	44	≥700	23	1.4	10.8
ConP	79.3°E	8.9°N	483	3.61 + 0.034/ −0.045	1.07	500	46	≥500	46	1.8	11.8
Apo	60.9°E	4.5°N	479	2.99 + 0.23/ −0.37	3.01	400	40	≥400	40	2.2	13.7
Dub	70.0°E	4.4°N	521	3.62 + 0.032/ −0.041	8.38	500	51	≥500	51	2.4	13.8
Firm	63.4°E	7.3°N	1332	3.27 + 0.10/ −0.21	3.4	400	109	≥500	59	3.0	15.5
WebbJ	64.0°E	0.6°S	289	3.66 + 0.035/ −0.047	1.37	500	35	≥500	35	2.4	14.4
Fec17	60.3°E	1.9°N	280	2.89 + 0.23/ −0.31	2.55	300	60	≥300	60	2.7	14.6
LP	61.9°E	7.9°N	663	3.37 + 0.097/ −0.24	4.33	500	35	≥500	35	2.8	14.6

Apo, show relatively thinner deposits than other typical crater mare units. Both are identified to contain minimum penetrated craters, with thickness estimates of 84–117 m for Firm and 62–77 m for Apo.

A total of ~4,200 fresh superposed impact craters were selected from the 66 basalt units for mare thickness estimation. Since superposed impact craters have to be large enough (which are much fewer than small craters) to be able to penetrate the surface mare deposits, they are observed on only 8 mare units (Fig. 10; Fig. S2). For each mare unit, the largest unpenetrated crater was used to constrain the lower limit of basalt thickness, except for the eight units containing minimum penetrating craters, where both the largest unpenetrated and smallest penetrating craters were considered. The estimated lower limits for mare thickness range from 41 to 207 m. It should be noted that these values represent lower-limit constraints rather than actual mare thicknesses. Larger mare units provide larger sampling areas and therefore have a higher probability of preserving larger impact craters capable of

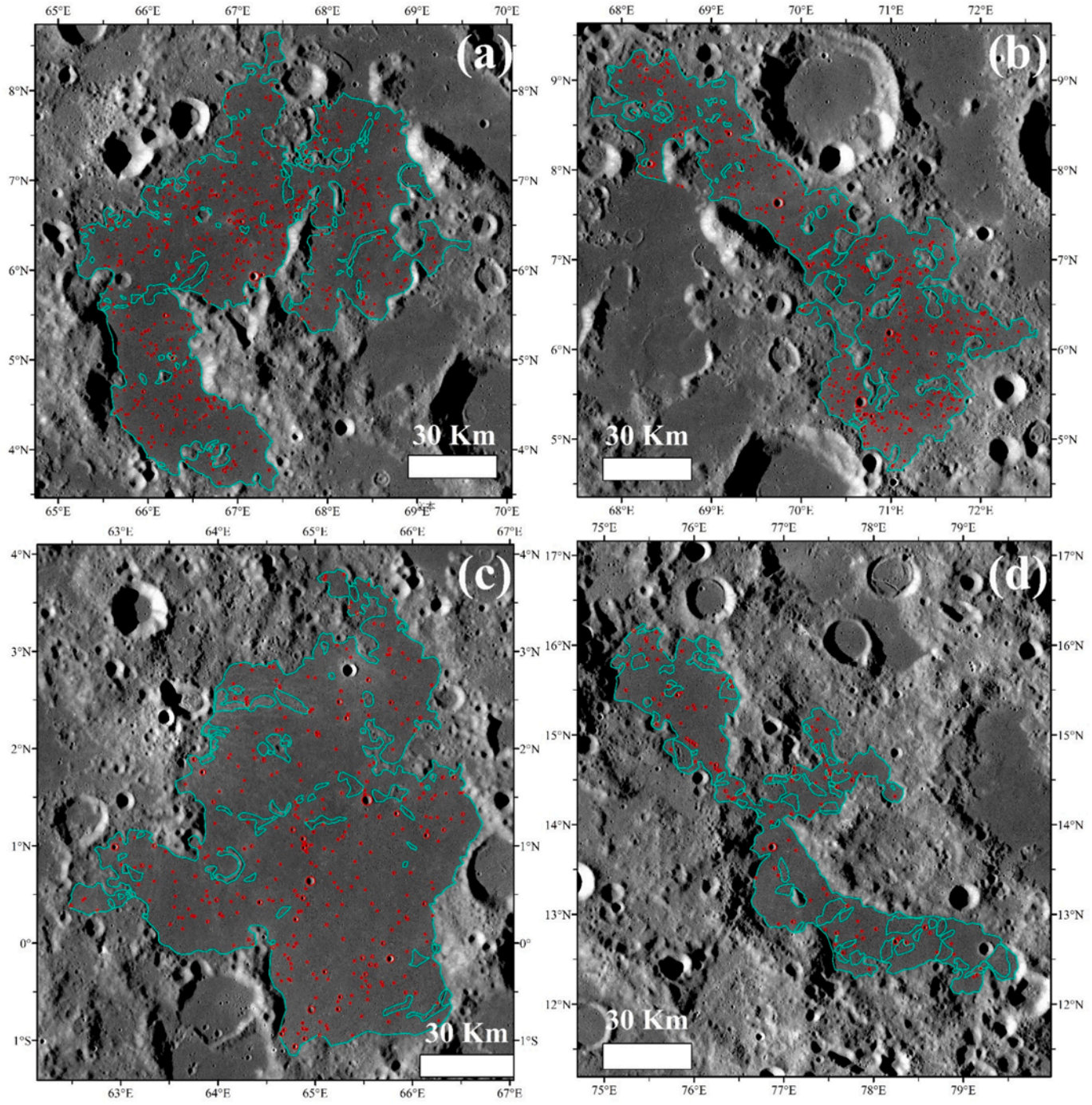


Fig. 8. Spatial distribution of counted superposed impact craters in the four largest mare units: panels a–d correspond to the units U2, U3, Sp1, and Ma6, respectively. The LROC WAC mosaic (100 m/pixel) was used as the base map.

penetrating deeper into the basalt layer. Consequently, the apparent relationship between mare unit size and estimated thickness may be partly influenced by crater sampling effects. Spatially, the estimated basalt thickness lower limits exhibit a distinct characteristic that larger mare units are characterized by greater thickness, whereas smaller mare units have relatively thinner basalt deposits (Fig. 10). Based on the basalt unit surface area, we further calculated that the total basalt volume in the entire study area is at least 7,000 km^3.

4.4. Mare basalt composition

4.4.1. Chemical composition

The FeO and TiO_2 abundances derived from remote sensing data represent the mean surface compositions of each mare unit. However, several factors may introduce uncertainties into these estimates. Impact-induced excavation can redistribute underlying materials, resulting in local compositional mixing between mare basalts and non-mare components. In addition, contamination from highland materials and impact ejecta, as well as variations in surface maturity, may affect the retrieved compositions. Furthermore, the spatial resolution of remote sensing data may cause subpixel mixing, particularly for small mare patches or

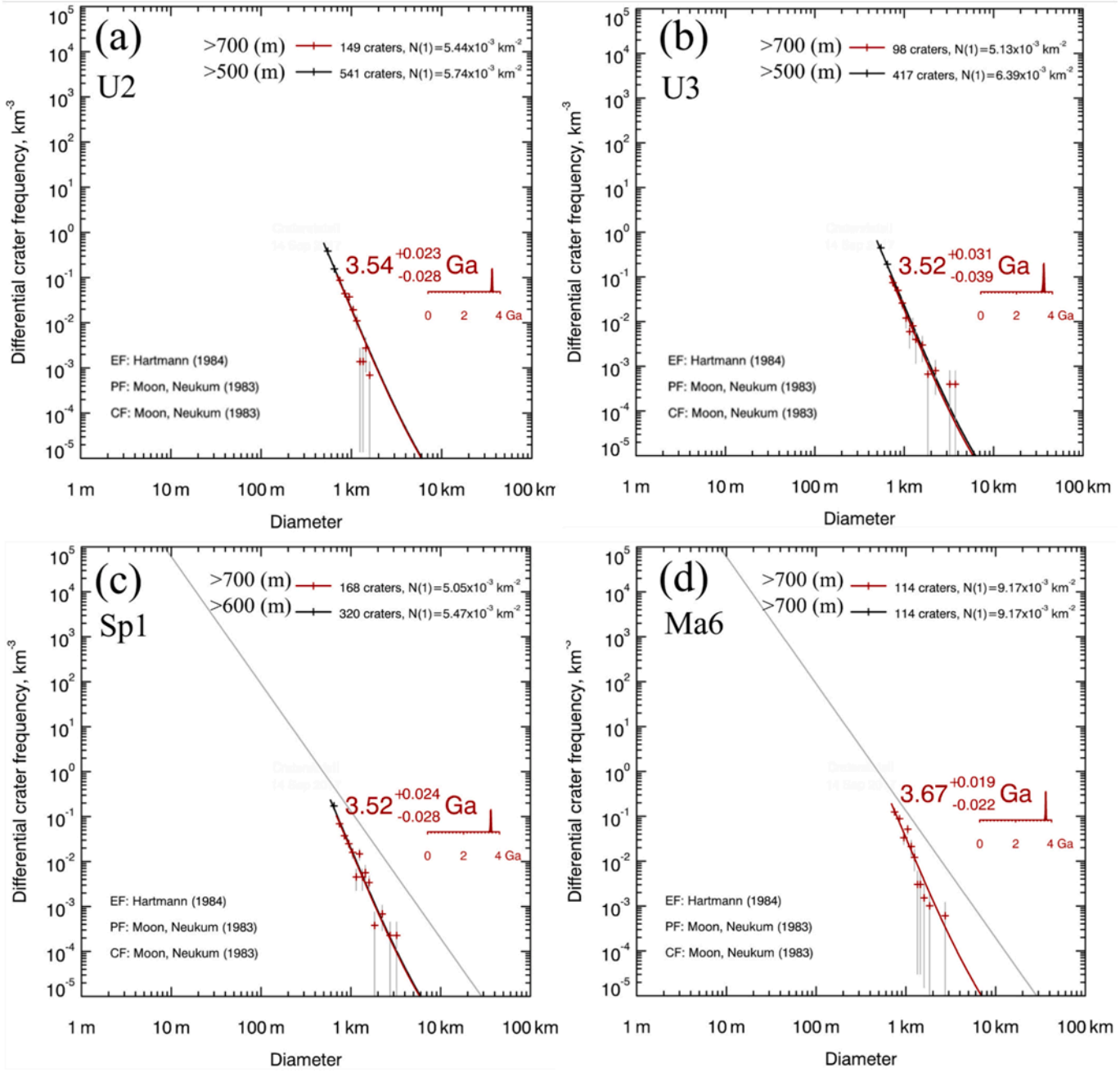


Fig. 9. Differential crater-size frequency distributions and derived absolute model ages (AMAs) for the four largest mare basalt units mapped within Mare Spumans, Mare Undarum, and the adjacent Mare Marginis (U2, U3, Sp1, and Ma6). Red curves indicate fitted crater populations, whereas black curves show the complete counted range. The CSFD plots and derived AMAs for the remaining 62 mare basalt units are provided in Table S1. (For interpretation of the references to colour in this figure legend, the reader is referred to the web version of this article.)

compositionally heterogeneous surfaces. Therefore, the derived FeO and TiO_2 values should be regarded as representative surface compositional estimates rather than the true bulk compositions of the basalt units.

Significant compositional differences, particularly the FeO content, are observed among all studied mare units (Table 1; Fig. 3b, 3c). First, mare units in the Mare Undarum region exhibit spatial heterogeneity in the composition of the several large mare units (Fig. 3b): the western U2 unit has the highest FeO content across the entire region (mean = 15.9 wt. %, 1σ = 2 wt. %), while the U3 (14.2 ± 2 wt. %) and several large adjacent basalt units in the east (U15, U16, ConP and ConF) have relatively lower FeO contents (mean value of 12.6 ± 1.3 wt. %). This reveals an east–west gradient in FeO content across the major mare units in the Mare Undarum region. The Condorcet crater floor mare (Con) exhibits a relatively flat surface (Fig. 3) and is characterized by lower FeO and TiO_2 compositions (mean FeO 11.6 ± 2.1 wt. %, mean TiO_2 1.9 ± 0.4 wt. %), compared to the major mare units in the Mare Undarum region.

The major mare unit Sp1 in Mare Spumans displays compositional homogeneity (mean FeO 15.2 ± 1.4 wt. %, mean TiO_2 3 ± 0.4 wt. %). A large impact crater (~4.3 km in diameter corresponding to an estimated excavation depth of ~0.9 km based on the topographic data, the crater depth was estimated from the elevation difference between the crater rim and the lowest point of the crater floor) in the northern portion of this unit is observed to have penetrated the surface mare, excavating and ejecting subsurface highland plagioclase materials to the surface surrounding this crater. The excavated subsurface materials are

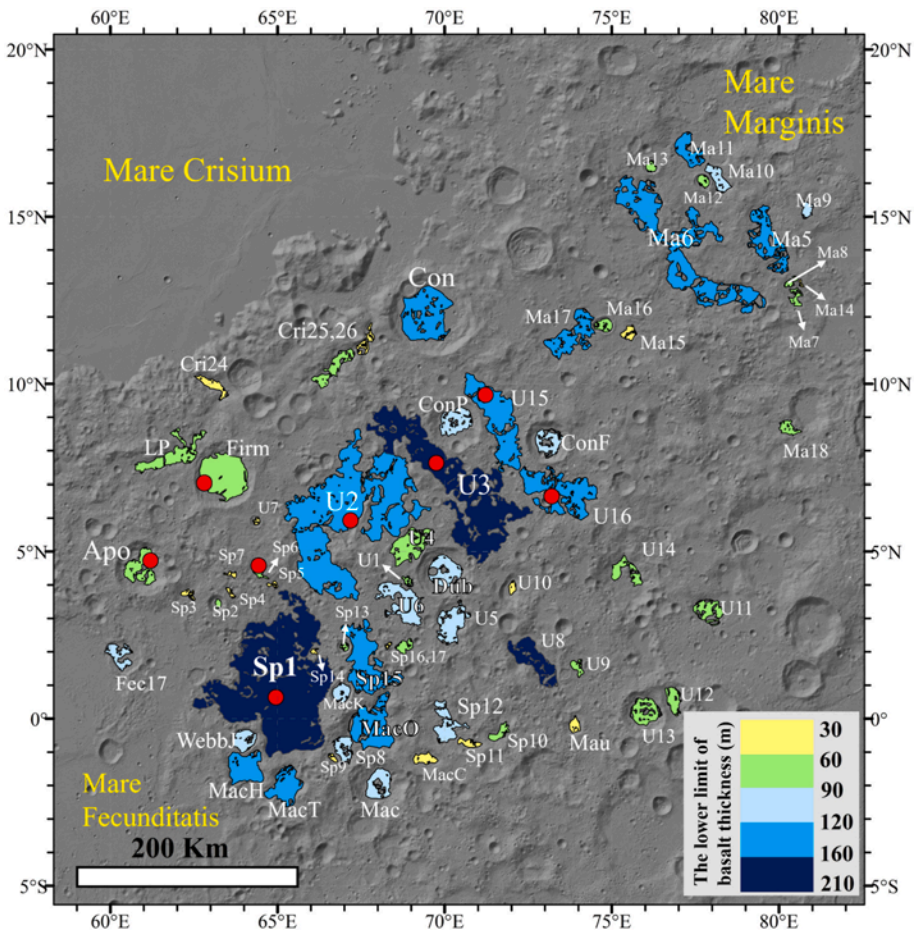


Fig. 10. Colour-coded map of the lower limit of basalt thickness (in meters) in each mare unit. The red dots denote the locations of the smallest penetrating craters identified in the 8 mare units. The locations and diameters of all largest non-penetrating and smallest penetrating craters are provided in Table S2 in the Supporting Information. Background grayscale map is a hillshade of the SLDEM2015 topography (256 pixels/degree). (For interpretation of the references to colour in this figure legend, the reader is referred to the web version of this article.)

characterized by obviously lower FeO and TiO_2 contents than the Sp1 mare basalt (Figs. 3b, 3c and 12c). Furthermore, several small mare units in the marginal portions of Maria Undarum and Spumans have relatively lower iron and titanium contents. For instance, several small units (Sp2, Sp3, Sp4, Sp7) north of Sp1 all exhibit FeO contents below 13 wt. % and TiO_2 contents below 2.5 wt. % (Table 1; Fig. 3a, 3b). In contrast, the LP and Firm mare units are compositionally similar to the southeastern Mare Crisium basalts, with relatively higher iron and titanium contents.

Significant differences in FeO and TiO_2 abundances are observed among the studied mare units. These variations may partly reflect different contributions of highland materials mixed with mare basalts, particularly in smaller or peripheral mare units. However, variations in the original FeO and TiO_2 abundances of the basaltic materials cannot be excluded. Therefore, the observed FeO and TiO_2 variations likely represent a combination of surface mixing effects and intrinsic differences in the FeO and TiO_2 abundances of mare basalts.

4.4.2. *Surface mineral abundance*

The four major rock-forming mineral abundance maps from Kaguya MI reveal that the basalts in the Maria Undarum and Spumans region are primarily composed of plagioclase (42–70 wt. %) and pyroxene (Cpx and Opx, 24–42 wt. %), and these maria are bounded by high-elevation, plagioclase-rich highlands (plagioclase: ~80–90 wt. %; pyroxene: generally <20 wt. %, typically ~5–15 wt. %). Our observations indicate that clinopyroxene (Cpx) is more abundant than orthopyroxene (Opx) in most mare units, with Cpx/Opx ratios consistently exceeding 1.6, consistent with a typical basaltic composition (Lucey, 2004; Papike et al., 1976). This result aligns with the pyroxene composition of basalts exposed along the southeastern margin of Mare Crisium, which is similarly dominated by Cpx (Lu et al., 2021). In addition, several small basalt units (U12, U13, U15, and Sp16) in the marginal portions exhibit a much lower Cpx/Opx ratio (<1.0), which is likely attributed to contamination by adjacent highland-derived materials.

The Firm mare unit exhibits the highest olivine content (~11 wt. %) among all studied 66 mare units in the Maria Undarum and Spumans region. By comparison, another relatively large mare (Con) emplaced on the floor of the Condorcet crater contains much less olivine (5 wt. %), but higher plagioclase abundance (58 vs. 46 wt. %). Furthermore, substantial mineralogical composition discrepancies exist between the eastern margin and other parts of the Con mare unit (Fig. 12c). Additionally, several small mare units (U9, U10, U14, Sp10, Sp11, Sp18 and Mac) along the southeastern margins of Maria Undarum and Spumans exhibit relatively lower olivine and pyroxene contents (Fig. 12c, d). These striking compositional contrasts suggest obvious mineral composition heterogeneity among these mare units or discrepant degrees of contamination by adjacent highland ejecta materials.

FeO and TiO_2 abundances exhibit a strong positive correlation ($r = 0.814$, $p < 0.001$; $R^2 = 0.663$; Table S5), indicating a consistent covariation between these two major compositional parameters. The linear regression analysis suggests that TiO_2 increases systematically with increasing FeO content, implying that iron-rich mare basalt units tend to contain higher TiO_2 abundances. In contrast, no statistically significant correlations are observed between AMAs and either FeO or

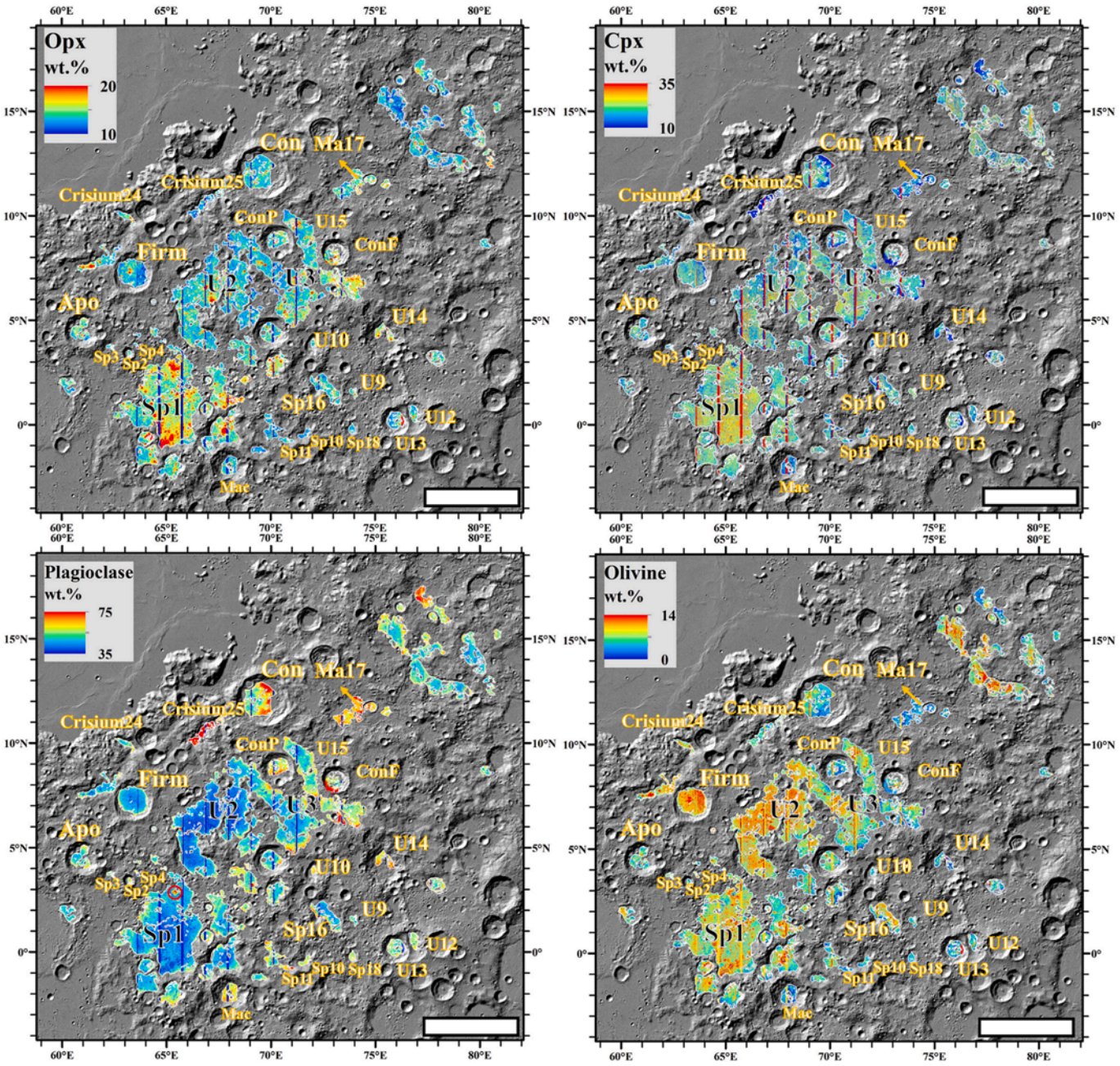


Fig. 12. Mineral abundance maps of the study maria obtained from the Kaguya MI-derived mineral abundance products (Lemelin et al., 2016): (a) orthopyroxene, (b) clinopyroxene, (c) plagioclase (the red circle outlines a large impact crater exhibiting spectral/geochemical anomalies), and (d) olivine. Unavoidable noise exists in the acquired image. (For interpretation of the references to colour in this figure legend, the reader is referred to the web version of this article.)

TiO_2 abundances. AMA–FeO and AMA–TiO_2 correlations show weak negative trends ($r = -0.293$, $p = 0.088$; $R^2 = 0.086$ and $r = -0.278$, $p = 0.107$; $R^2 = 0.077$, respectively), indicating that the surface ages of mare basalt units alone do not explain their compositional variations. These weak relationships likely reflect the combined effects of mantle source characteristics, magma generation processes, and local geological environments.

5. Discussion

5.1. FeO and TiO_2 variations of the Maria Undarum and Spumans basalts

Given that some small basalt units, particularly those adjacent to highlands, are heavily contaminated by impact ejecta of feldspathic composition (Gillis-Davis et al., 2006), 31 small mare units (Cri24–-Cri26, Ma7, Ma10–Ma17, Mac, MacK, Sp2–Sp7, Sp9, Sp10, Sp11, Sp13, Sp16–Sp18, U1, U10, U11, U14) were excluded from the compositional analysis in this subsection. The average TiO_2 contents of the remaining 35 basalt units range from 1.9 ± 1.7 to 3.4 ± 3.7 wt. %, while the average FeO contents range from 11.6 ± 2.3 to 15.9 ± 2.1 wt. %. Furthermore, the main large units (U2, U3, Sp1) of Maria Spumans and Undarum are notably higher in elemental abundance compared to the surrounding smaller mare units (e.g., U12, U16, Sp12 and Con; Fig. 13b). This difference may partly reflect the larger extent of major mare units, whose central regions are generally farther from surrounding highland materials and thus less affected by highland contamination. Furthermore, the observed compositional variations may reflect a combination of primary basalt heterogeneity and mixing with highland

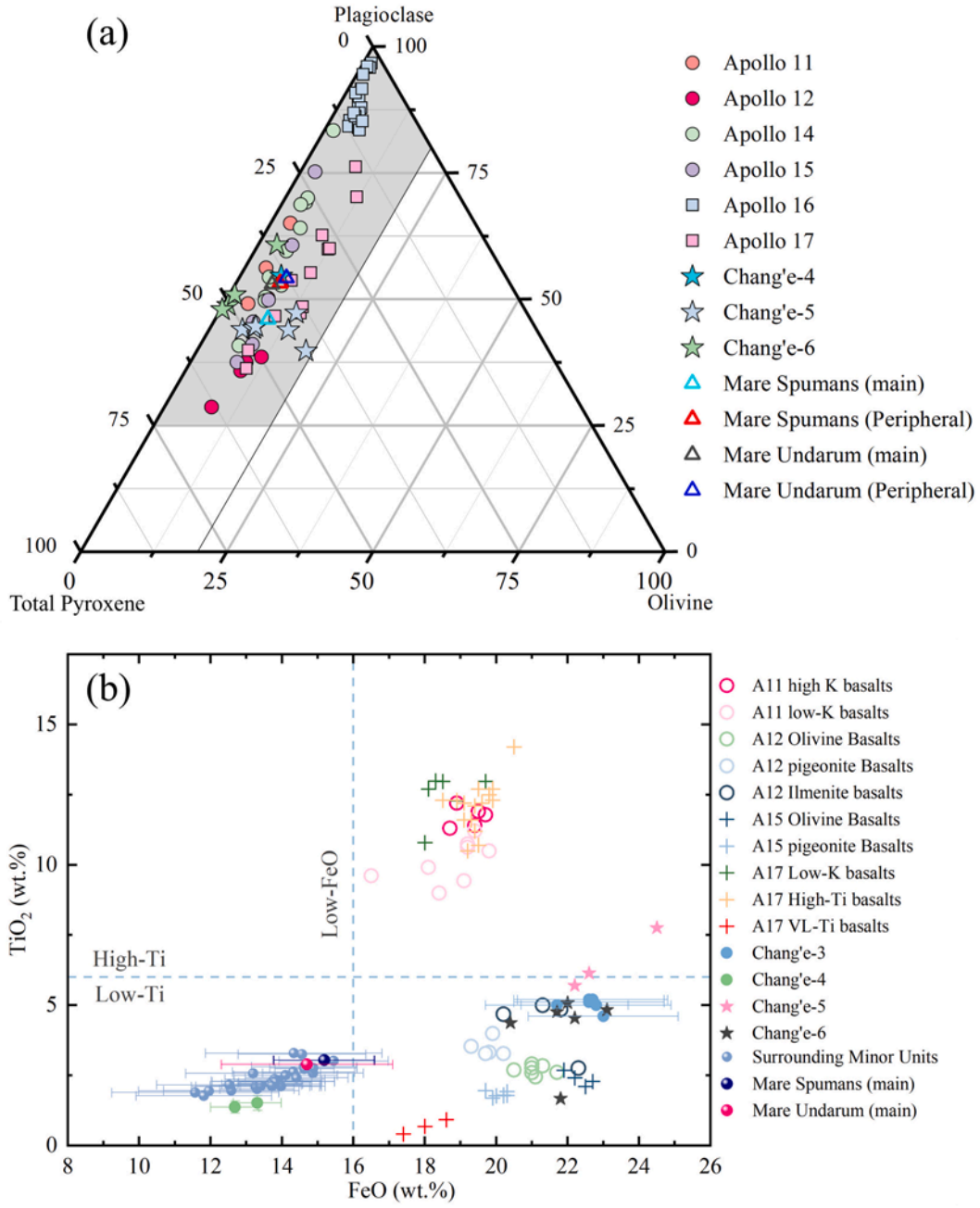


Fig. 13. (a) Triangular plot of major mineral abundances. Apollo and Luna soils are sourced from Taylor et al. (2001, 2010). The Chang'e-4 mission landing site is derived from Qiao et al. (2019). Chang'e-5 and Chang'e-6 missions are obtained from Li et al. (2022, 2024), respectively. All mineral composition data points used for comparison are provided in Table S3 in Supporting Information. The light blue and black triangles represent the main Sp1 unit of Mare Spumans and the principal U2 and U3 units of Mare Undarum, respectively; the red and dark blue triangles denote the remaining basaltic units of Mare Spumans and Mare Undarum. (b) Comparison of FeO and TiO_2 abundances in mare basalts from Maria Undarum and Spumans with those of all typical lunar mare basalt samples returned by the Apollo and Luna Missions (Error bars denote 1σ uncertainties; Lucey et al., 2006). Mare basalts at the Chang'e-6 landing site are sourced from Li et al. (2024), Wang et al. (2025a), and Wang et al. (2025b). Chang'e-5 mission soils are derived from Tian et al. (2021) and Che et al. (2021), while surface in-situ geochemical measurement data for Chang'e-3 are from Ling et al. (2015). The dark blue circles represents Sp1, the pink circles denotes the mean of U2 and U3, and the light-colored circles represent the remaining 32 units. (For interpretation of the references to colour in this figure legend, the reader is referred to the web version of this article.)

materials. Although fresh impact craters can provide constraints on subsurface compositions, most craters in the study area excavate only shallow materials, and relatively few penetrating craters are available for analysis. Therefore, the potential influence of deeper or buried materials cannot be fully constrained.

The FeO contents of these mare units are obviously lower than those of all returned lunar basalt samples (Fig. 13b). Their mineral compositions also show relatively higher plagioclase and lower mafic mineral (olivine and pyroxene) abundances compared with Apollo samples (Fig. 13a). These differences should be interpreted with caution because orbital remote-sensing data and returned samples represent different measurement scales and sampling conditions. Returned samples provide detailed compositional information but are restricted to localized sites, whereas orbital observations characterize larger surface areas and may be influenced by subpixel mixing, surface contamination, and uncertainties in spectral inversion. Therefore, the low-Fe and low-Ti

characteristics of the Maria Undarum and Spumans basalts may reflect intrinsic basalt heterogeneity, variable highland material mixing, or a combination of both processes. Similarities with the Chang'e-4 landing site basalts (Qiao et al., 2019) indicate comparable low-FeO and low-TiO_2 characteristics, although the relative contributions of primary basalt variability and highland material mixing remain uncertain (Giguere et al., 2000).

In previous studies, positive correlations between FeO and TiO_2 abundances have been documented in relatively Fe- and Ti-rich mare basalts, such as those in the Mare Imbrium (Bugiolacchi and Guest, 2008). However, such a correlation has not been thoroughly examined in low-titanium mare regions. Based on our compositional analyses, FeO and TiO_2, we also identify a positive correlation between FeO and TiO_2 contents across the mare units in the Maria Undarum and Spumans region (Fig. 14a). This correlation reflects the coupled behavior of FeO and TiO_2 during lunar basalt evolution, as both are influenced by the crystallization and fractionation of Fe- and Ti-bearing minerals during magma differentiation (Head, 1976; Shearer and Papike, 1999; Elkins-Tanton et al., 2011). Previous studies on the composition-age relationship of lunar mare basalts have primarily focused on young units, suggesting that FeO and TiO_2 in lunar basalts have become progressively enriched over time (Bugiolacchi et al., 2006; Qian et al., 2021; Wang et al., 2025a). However, this temporal composition trend has rarely been documented in ancient mare units. For the 35 ancient basalt units analyzed in this study, no statistically significant correlations are identified between AMA and either FeO or TiO_2 abundances. Although weak negative trends are observed for AMA–FeO ($r = -0.293$, $p = 0.088$) and AMA–TiO_2 ($r = -0.278$, $p = 0.107$; Table S5), these relationships do not

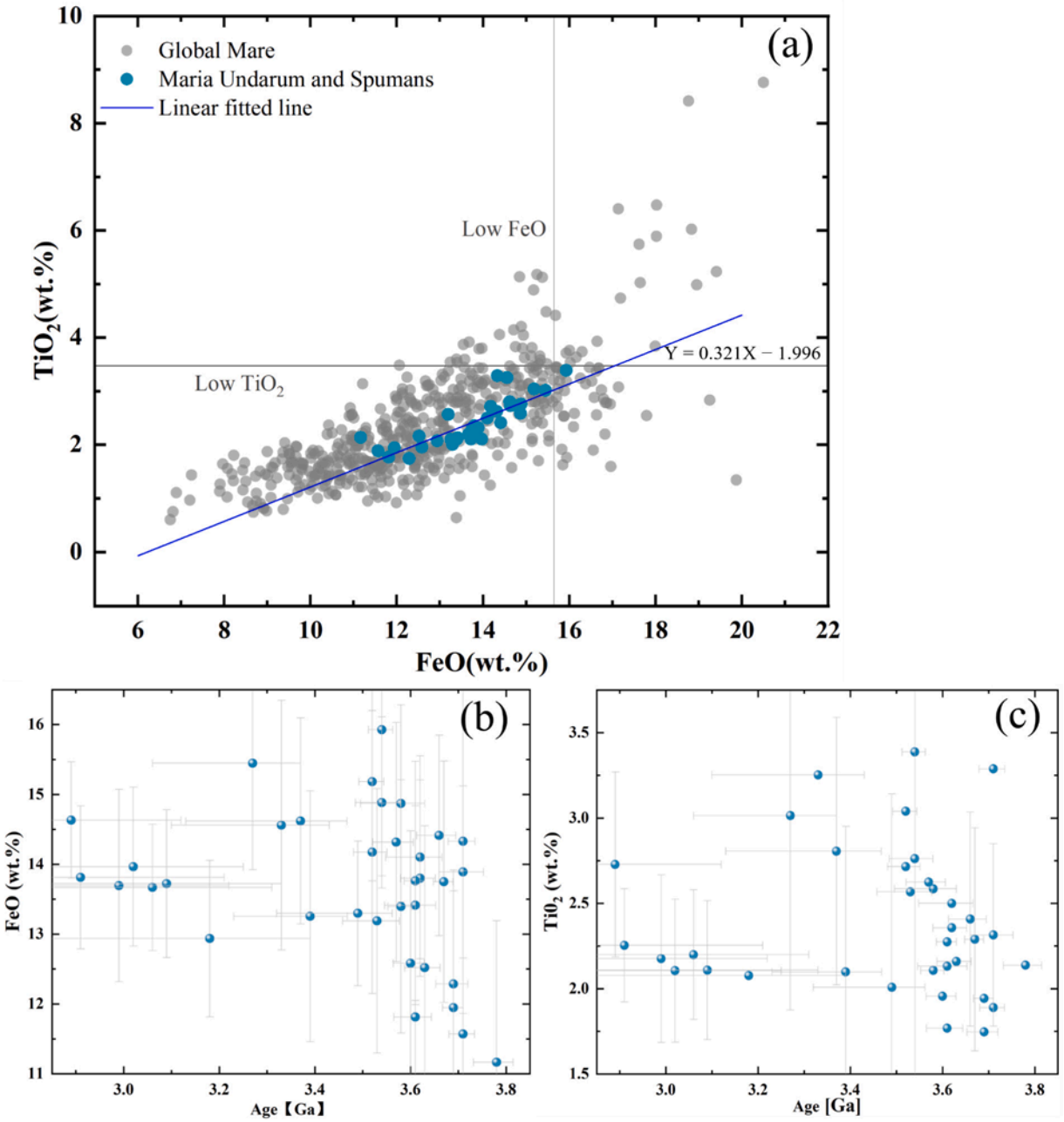


Fig. 14. (a) A plot of mean FeO and TiO_2 contents of the 35 mare units in the Maria Undarum and Spumans region, and previously dated mare units (Fig. 1). Plots of (b) FeO and (c) TiO_2 contents against age of mare units in the Maria Undarum and Spumans region. The gray error bars represent the standard deviations (SDs) of the extracted mean FeO and TiO_2 abundances within each mare basalt unit.

indicate a systematic age-dependent variation in basalt composition. Therefore, the mare deposits in the study region do not show a clear compositional evolution pattern with time. Nevertheless, the scatter plots show a tendency for younger units to exhibit relatively lower TiO_2 abundances and a narrower range of FeO variations compared with older units (Fig. 14b, 14c).

5.2. Mare thickness (lower limit values) distribution of the Maria Undarum and Spumans basalts

Mare thickness distribution map (Fig. 10) demonstrates that, with the exception of several large mare units (e.g., U2, U3, U15, U16, Sp1, Sp15), the many small basalt units (e.g., U7, U10, Sp3, Sp5, Sp7, Sp9) are consistently characterized by thin basalts. These small mare units collectively form a thin, discontinuous annular veneer encircling the main large mare units in the Maria Undarum and Spumans region. Such a distribution may reflect the influence of the pre-existing impact basin topography on basalt accumulation, as mare basalts commonly pond within topographic depressions of impact basins (De Hon, 1979; Head, 1976; Solomon and Head, 1980). However, the effects of magma flow dynamics, cooling conditions, and possible subsidence on the observed thickness variations cannot be quantitatively constrained with the data employed in this work.

Based on the global lunar crustal thickness model constructed from gravity field measurements (Wieczorek et al., 2013), we find that the lunar crusts in Maria Crisium and Smythii regions are anomalously thin. The crustal thickness of some regions of Mare Crisium even approaches 0. In contrast, the lunar crust of Maria Undarum and Spumans is much thicker (~35 km) than that of the two adjacent maria (Crisium and Smythii). Notably, Maria Crisium and Smythii experienced extensive mare infilling, whereas Maria Undarum and Spumans were characterized by small-scale and sporadic mare infilling. This phenomenon may partly reflect variations in crustal structure, as thicker crust can hinder large-scale magma ascent and eruption (Head, 1976; Head and Wilson, 1992). However, crustal thickness alone cannot fully explain the extent of mare volcanism. The volume and distribution of mare basalts are also influenced by magma supply, mantle melting conditions, lithospheric thermal evolution, and structural controls on magma pathways (Solomon and Head, 1980; Elkins-Tanton et al., 2011). Therefore, the limited and scattered mare deposits in Maria Undarum and Spumans likely result from the combined effects of crustal structure and volcanic processes.

5.3. The geological evolution history of the Maria Undarum and Spumans region

On the basis of the chronological constraints, lower-limit thickness estimates, and FeO and TiO_2 abundance variations presented above, the geological evolution history of the Maria Undarum and Spumans region is interpreted to be composed of four major stages (Fig. 15): (1) large basin-forming impacts and basin ejecta emplacement, (2) early major-phase mare volcanism, (3) the subsequent gradual decline of mare volcanic activity, and (4) post-mare geological modifications. The detailed geological evolutionary history of each stage is outlined as follows:

(1) The Maria Undarum and Spumans regions are situated on the periphery of the outer main ring structure of the Crisium basin (Fig. 5), which formed approximately 3.9–4.1 Ga ago (Wilhelms, 1987; Stöffler and Ryder, 2001; Orgel et al., 2018). The Crisium basin also produced the extensive exterior ejecta blanket terrains, which are topographically very hummocky and composed of many massifs and depressions. These depressions, along with subsequent major impact craters (e.g., Condorcet and Firmicus)

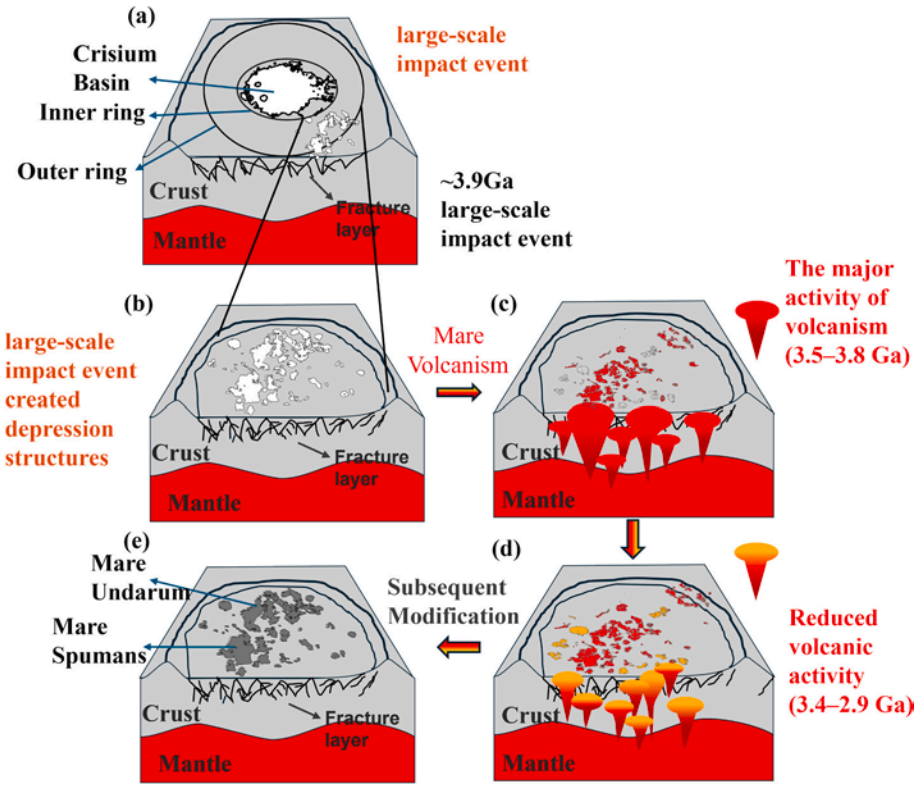


Fig. 15. Schematic diagram of the geological evolution history of the Maria Undarum and Spumans region. (a, b) The large-scale impact event that formed the Crisium basin not only generated the main Crisium basin itself, but also created a series of depression structures (white patches). (c, d) These depressions were subsequently infilled by mare basalt volcanism, including widespread emplacement during the main phase of volcanic activity and subsequent waning volcanism. (e) Subsequent modifications involve continuous impact cratering and space weathering processes up to the present.

(Fig. 6; Fig. 15a, 15b), provided the topographic settings for accommodating subsequent mare fillings.

(2) Based on the estimated minimum volumes and AMAs of the mare units in the Maria Spumans and Undarum region (Fig. 7 and Fig. 11b), it is evident that during the late Imbrian epoch (3.8–3.2 Ga), extensive mare volcanic eruptions occurred in this region. Effusive lava flows preferred to be emplaced on the floors of pre-existing topographic depressions in the basin ejecta blanket and subsequent (superposed on the basin units) large impact craters, forming the observed irregularly shaped and chemically homogeneous mare plains and patches in this region. The earliest small-scale volcanic eruptions in this region initiated approximately 3.7 Ga ago, which mainly occurred in the marginal portions of the Maria Undarum and Spumans region (units U8, Con, Ma8, and Ma9). Over the subsequent period of about 0.3 Ga (3.7–3.5 Ga), the erupted basaltic lava flows formed the majority of the mare units in the Maria Undarum and Spumans region (e.g., the four largest mare units: Sp1, U2, U3, and Ma6), with a major eruption period at around 3.5 Ga. These major-phase late Imbrian basaltic deposits, especially the large-scale regions, are characterized by higher FeO, TiO_2, olivine and pyroxene contents (especially clinopyroxene) and lower plagioclase contents (Fig. 3b, 3c; Fig. 12 and Fig. 13).

(3) Following the main phase of volcanism, volcanic activity gradually declined during the subsequent interval (~3.4–2.9 Ga), as indicated by the smaller exposed basalt volumes of younger units. Within this period, large-scale volcanic activity had essentially ceased; only smaller-scale basaltic lava flows were erupted and filled the floors of some small depressions and impact craters, where sufficient accommodation space was available for lava accumulation. These younger basalt units were primarily located in the western and southeastern parts of the Maria Undarum and Spumans region (e.g., units Firm and Apo, Fec17, U7, Sp3, Sp4, Sp10 and Sp11), covering a total area of approximately 4,293 km^2. Compared with the major mare units (e.g., Sp1, U2, and U3), these younger units exhibit relatively lower FeO and TiO_2 abundances, although their surface compositions are broadly similar to each other.

(4) Approximately 2.9 Ga ago, volcanism in the Maria Undarum and Spumans region generally ceased. Surface modification has since been dominated by meteoritic bombardment and space weathering, which generated abundant small superposed impact craters and continuous regolith development. A representative crater formed during this period is the bright-rayed crater Petit in the west of Mare Spumans (Fig. 2; Fig. 6a), whose optically fresh ejecta system records a post-mare impact event.

The evolutionary history of the Maria Undarum and Spumans region epitomizes the typical evolution path of the outer annulus of Crisium basin (Wilhelms, 1987; Spudis et al., 1989; Hiesinger et al., 2003): a huge impact-generated structural setting, modified by localized small-scale basaltic resurfacing, followed by prolonged magmatic quiescence. Although limited in areal extent compared to the major lunar maria (e.g., Maria Crisium and Imbrium), their well-preserved stratigraphic architecture and discrete volcanic signatures provide important constraints on small-scale mare volcanism and post-impact volcanic evolution within the outer annulus of the Crisium basin.

5.4. *Age comparison with the global Moon and adjacent maria*

The 14 Mare Marginis units (Ma5–Ma18) identified in this study have model ages ranging from 3.33 to 3.78 Ga, with an area-weighted mean age of ~3.57 Ga. This value is comparable to the previously reported mean age of 3.62 Ga for Mare Marginis (Hiesinger et al., 2011a), supporting the consistency of our CSFD-derived ages with previous studies. Similarly, the three basalt units (Cri24–Cri26) identified on the southeastern periphery of Mare Crisium yield an area-weighted mean age of 3.49 Ga, consistent with CSFD-derived ages of 3.49–3.74 Ga reported by Lu et al. (2021), although slightly older than sample-based ages from Mare Crisium (Vaniman and Papike, 1977; Fernandes and Burgess, 2005).

Based on the dating results obtained by previous researchers (Hiesinger et al., 2006, 2011a, 2011b; Morota et al., 2009, 2011; Whitten et al., 2011; Cho et al., 2012; Haruyama et al., 2009; Trieloff et al., 1998; Pasckert et al., 2015, 2018; Jin et al., 2025), we compiled the ages of ~500 mare basalt units across the Moon and 48 units in the vicinity of the Maria Undarum/Spumans region, and compared them with the mare ages obtained in this work (Fig. 16 a–d). The model ages of the 48 adjacent mare units (including units in Maria Crisium, Fecunditatis, Smythii, and Marginis, as well as crater-floor basaltic units in the nearby Goddard (CGo1), Hubble (CHu1), and Joliot (CJo1 and CJo2) craters; Table S4) range from 2.7 to 3.8 Ga, with a predominant occurrence between 3.5 and 3.7 Ga, and a distinct concentration around 3.5 Ga. The ages of the basalt units in the Maria Undarum/Spumans

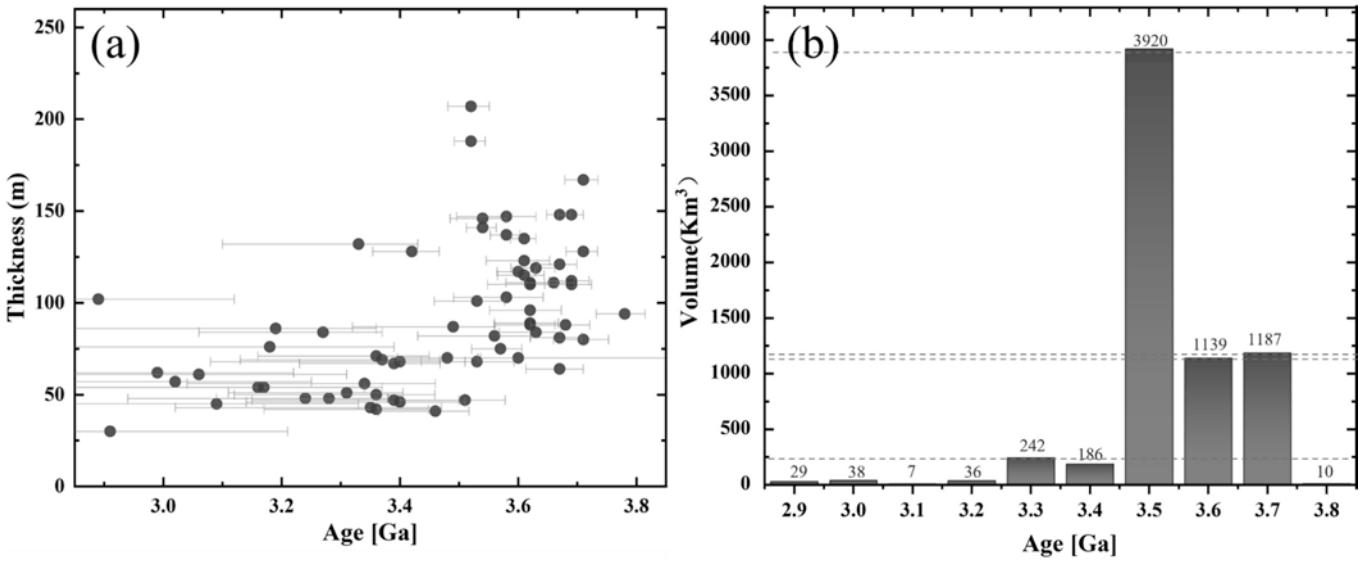


Fig. 11. (a) Relationship between the estimated lower limits of mare basalt thickness and AMAs and (b) histogram showing the variation of exposed mare basalt volumes with AMAs.

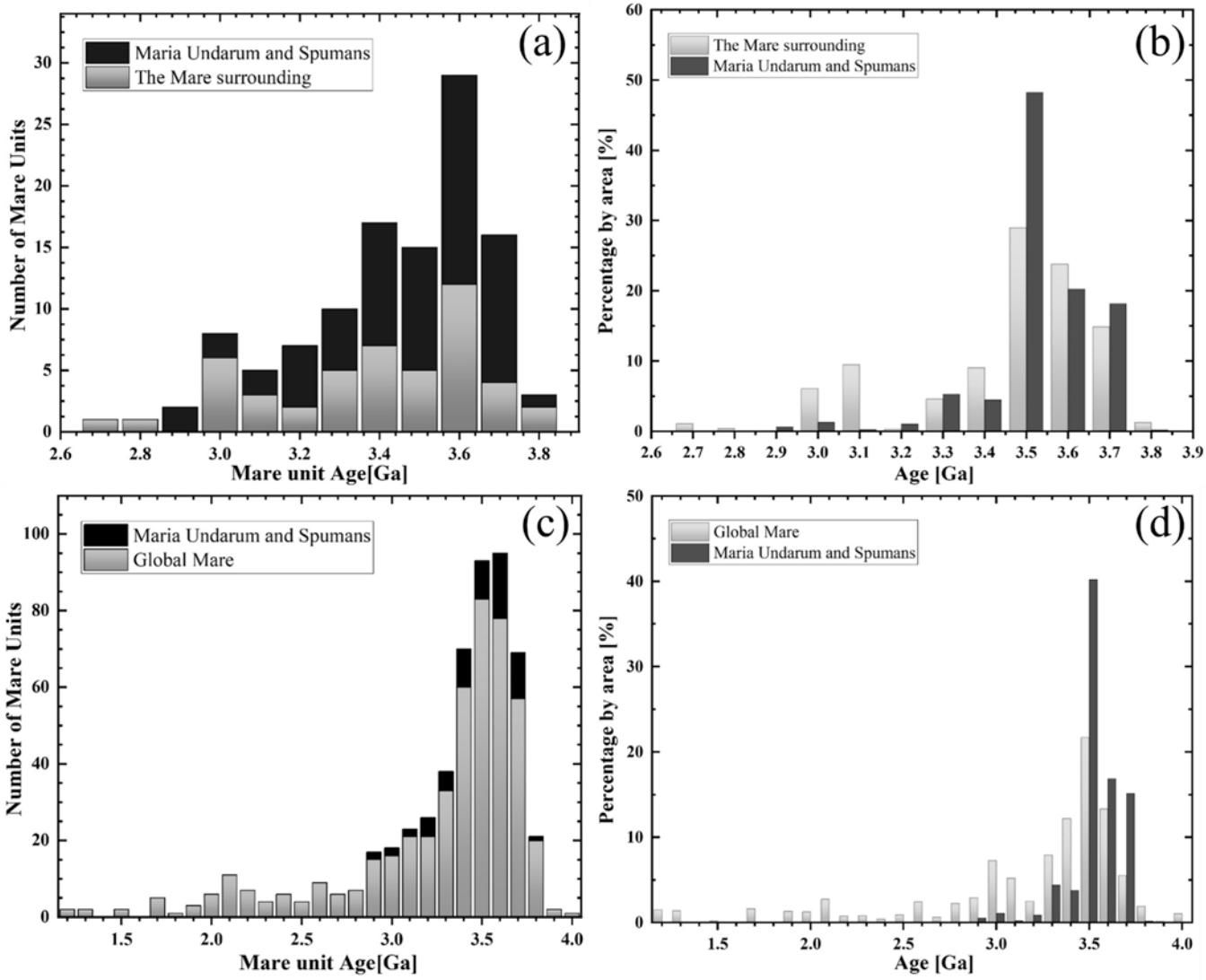


Fig. 16. (a) Age frequency and (b) areal proportions of basaltic units by geological age comparisons between the Maria Undarum/Spumans region and neighboring maria. (c) Age frequency and (d) areal percentages of mare basaltic units in each age bin, comparing global lunar maria with the Maria Undarum/Spumans region.

region span from ~2.9 to 3.8 Ga, with most units concentrated between 3.5 and 3.8 Ga, while a few younger units indicate continued but diminished basalt emplacement during the later period (2.9–3.4 Ga, Fig. 11b). The exposed basalt surfaces show enhanced emplacement activity during 3.5–3.7 Ga, with a pronounced concentration of surface emplacement ages ~3.5 Ga, similar to those of the surrounding mare units. Global lunar mare basalt surfaces with available model ages are mainly concentrated between 3.3 and 3.8 Ga (Fig. 16c, 16d). This interval includes 331 dated basalt units and accounts for approximately 62.6% of the total mapped mare basalt area (2,758,168 km^2 out of 4,404,862 km^2). This distribution indicates that a large proportion of the currently exposed mare surfaces were emplaced during this period. The concentration of surface emplacement ages ~3.5 Ga represents the timing of major resurfacing events recorded at the surface. The subsequent decrease in younger surface ages reflects localized late-stage volcanic activity during the waning phase of lunar magmatism, consistent with the overall decline in mare basalt emplacement associated with progressive interior cooling, reduced mantle melting, and decreasing magma supply (Hiesinger et al., 2011a; Head and Wilson, 2017). The Maria Undarum and Spumans region therefore represents a peripheral expression of this prolonged decline in lunar mare volcanism.

Nevertheless, the Maria Undarum and Spumans region lacks mare units younger than ~3.0 Ga, indicating that large-scale basaltic volcanism did not continue into the late lunar history in this region. This pattern may reflect the combined influence of regional crustal structure, magma supply, and magma ascent pathways. Unlike mare deposits within large impact basins, Maria Undarum and Spumans are located along the exterior of the Crisium multi-ring basin, where elevated topography and relatively thicker crust may have limited prolonged basaltic emplacement.

By comparing our results with the chronologies of global mare volcanism, we infer that small volcanic eruptions in lunar regions of a thick crust predominantly occurred during the early history of the Moon. These findings provide novel insights into the global thermal evolution of the Moon. The Maria Undarum and Spumans region, located along the outer annulus of the Crisium multi-ring basin, provides an important example for investigating how basin-related crustal structures and crustal thickness variations influenced the spatial and temporal evolution of localized basalt emplacement. These results provide additional constraints on the volcanic evolution of lunar impact basins and the factors controlling mare basalt distribution.

6. Conclusions

In this work, we investigated the chronological and compositional characteristics of 66 basalt units in the Maria Undarum and Spumans region. Absolute model ages ranging from ~2.9 to 3.8 Ga were derived from crater size–frequency distribution analysis. In addition, FeO, TiO_2, and major mineral abundance data were analyzed to characterize the compositional variations among these basalt units. Based on the compositional maps, we found that although the regional mare volcanism is dominated by low-Ti basalts, compositional heterogeneity still exists among the 66 mare units. Additionally, the crater excavation depth method was used to constrain the lower limits of the exposed basalt thickness (~41 m to 207 m) in this region. Combining the temporal variation of the total eruption volume and compositional variations, we suggest that volcanic activity in the region was dominated by extensive eruptions during the early stage (~3.8–3.5 Ga), followed by progressively waning volcanic activity from ~3.4 to 2.9 Ga. Moreover, no clear correlation is observed between basalt composition and age although younger basalts show lower titanium contents and a narrower iron compositional range than older basalts. Therefore, the mare deposits in the study region do not show a clear compositional evolution pattern with time. Finally, comparison with the ages of global lunar volcanism demonstrates that small-scale volcanic eruptions outside major impact basins are generally very ancient (>3.5 Ga), characterized by short durations, irregular mare outlines, small eruptive volumes, and emplacement within topographic depressions in highland terrains.

CRediT authorship contribution statement

Jingdong Zhang: Writing – review & editing, Writing – original draft, Visualization, Validation, Methodology, Investigation, Formal analysis, Data curation, Conceptualization. **Yuzheng Zhang:** Writing – review & editing, Methodology. **Jian Chen:** Writing – review & editing, Methodology. **Luyuan Xu:** Writing – review & editing, Methodology. **Le Qiao:** Writing – review & editing, Writing – original draft, Validation, Supervision, Project administration, Methodology, Investigation, Funding acquisition, Formal analysis, Conceptualization.

Declaration of competing interest

The authors declare that they have no known competing financial interests or personal relationships that could have appeared to influence the work reported in this paper.

Acknowledgments

This work is supported by the National Natural Science Foundation of China (42441817, 42578002, and 42241107), State Key Laboratory of Lunar and Planetary Sciences, Macau University of Science and Technology (002/2024/SKL), Science and Technology Development Fund of Macau (0012/2023/RIA1), and Fundamental Research Funds for the Central Universities (501XYGG2026158010).

Appendix A. Supplementary data

Supplementary data to this article can be found online at https://doi.org/10.1016/j.icarus.2026.117372.

Data availability

All the original Kaguya/SELENE (MI and TC) data are archived at SELENE Data Archive (https://darts.isas.jaxa.jp/app/pdap/selene/), original LRO (WAC and LOLA) and SLDEM2015 topography data can be found in the NASA Planetary Data System Geosciences Node (https://pds-geosciences.wustl.edu/), and the MI mineral abundance maps are available at Astropedia Lunar and Planetary Catalog (https://astrogeology.usgs.gov/search/map/kaguya_lunar_multiband_imager_59mpp). The corresponding GIS shapefiles are available through the LROC GIS data archive (https://data.lroc.im-ldi.com/lroc/view_rdr/SHAPEFILE_LROC_GLOBAL_MARE). The basalt unit boundaries and crater counting data used in this study are available at Zenodo (https://doi.org/10.5281/zenodo.21967255).

References

Andersson, L.E., Whitaker, E.A., 1982. NASA Catalogue of Lunar Nomenclature, 1097. NASA Reference Publication.
Baldwin, R.B., 1974. Was there a "terminal lunar cataclysm" 3.9–4.0×10^9 years ago? Icarus 23, 157–166. https://doi.org/10.1016/0019-1035(74)90003-7.
Barker, M.K., Mazarico, E., Neumann, G.A., Zuber, M.T., Haruyama, J., Smith, D.E., 2016. A new lunar digital elevation model from the Lunar Orbiter Laser Altimeter and SELENE Terrain Camera. Icarus 273, 346–355. https://doi.org/10.1016/j.icarus.2015.07.039.
Basilevsky, A., Neukum, G., Nyquist, L., 2010. The spatial and temporal distribution of lunar mare basalts as deduced from analysis of data for lunar meteorites. Planet. Space Sci. 58, 1900–1905. https://doi.org/10.1016/j.pss.2010.08.020.
Bennett, K.A., et al., 2016. Complex explosive volcanic activity on the moon within Oppenheimer crater. Icarus 273, 296–314. https://doi.org/10.1016/j.icarus.2016.02.007.
Borg, L.E., Shearer, C.K., Asmerom, Y., Papike, J.J., 2004. Prolonged KREEP magmatism on the Moon indicated by the youngest dated lunar igneous rock. Nature 432, 209–211. https://doi.org/10.1038/nature03070.
Bugiolacchi, R., Guest, J.E., 2008. Compositional and temporal investigation of exposed lunar basalts in the Mare Imbrium region. Icarus 197, 1–18. https://doi.org/10.1016/j.icarus.2008.04.001.
Bugiolacchi, R., Spudis, P.D., Guest, J.E., 2006. Stratigraphy and composition of lava flows in Mare Nubium and Mare Cognitum. Meteorit. Planet. Sci. 41, 285–304. https://doi.org/10.1111/j.1945-5100.2006.tb00210.x.
Che, X., et al., 2021. Age and composition of young basalts on the Moon, measured from samples returned by Chang'e-5. Science 374, 887–890. https://doi.org/10.1126/science.abl7957.
Cho, Y., Morota, T., Haruyama, J., Yasui, M., Hirata, N., Sugita, S., 2012. Young mare volcanism in the Orientale region contemporary with the Procellarum KREEP Terrane (PKT) volcanism peak period~ 2 billion years ago. Geophys. Res. Lett. 39, L11203. https://doi.org/10.1029/2012GL051838.
Clark, P., Hawke, B., 1987. The relationship between geology and geochemistry in the Undarum/Spumans/Balmer region of the Moon. Earth Moon Planet. 38, 97–112. https://doi.org/10.1007/BF00119678.
De Hon, R., 1975a. Mare Spumans and Mare Undarum: structural and depositional history. In: Abstracts of the Lunar Planet. Sci. Conf., 6, p. 181.
De Hon, R., 1975b. Mare Spumans and Mare Undarum-Mare thickness and basin floor. In: Lunar Sci. Conf., 6, pp. 2553–2561.
DeHon, R.A., 1979. Thickness of western mare basalts. In: Proc. Lunar Planet. Sci. Conf. 10th (1979), pp. 2935–2955.
Elkins-Tanton, L.T., Burgess, S., Yin, Q.-Z., 2011. The lunar magma ocean: reconciling the solidification process with lunar petrology and geochronology. Earth Planet. Sci. Lett. 304, 326–336. https://doi.org/10.1016/j.epsl.2011.02.004.
Fernandes, V.A., Burgess, R., 2005. Volcanism in mare fecunditatis and mare crisium: Ar-Ar age studies. Geochim. Cosmochim. Acta 69, 4919–4934. https://doi.org/10.1016/j.gca.2005.05.017.
Garrick-Bethell, I., Head III, J.W., Pieters, C.M., 2011. Spectral properties, magnetic fields, and dust transport at lunar swirls. Icarus 212, 480–492. https://doi.org/10.1016/j.icarus.2010.11.036.
Giguere, T.A., Taylor, G.J., Hawke, B.R., Lucey, P.G., 2000. The titanium contents of lunar mare basalts. Meteorit. Planet. Sci. 35, 193–200. https://doi.org/10.1111/j.1945-5100.2000.tb01985.x.
Gillis, J.J., Spudis, P.D., 2000. Geology of the Smythii and Marginis region of the Moon: using integrated remotely sensed data. J. Geophys. Res. 105, 4217–4233. https://doi.org/10.1029/1999JE001111.
Gillis-Davis, J.J., Lucey, P.G., Hawke, B.R., 2006. Testing the relation between UV–vis color and TiO_2 content of the lunar maria. Geochim. Cosmochim. Acta 70, 6079–6102. https://doi.org/10.1016/j.gca.2006.08.035.
Haruyama, J., et al., 2008. Global lunar-surface mapping experiment using the Lunar Imager/Spectrometer on SELENE. Earth Planet. Space 60, 243–255. https://doi.org/10.1186/BF03352788.
Haruyama, J., et al., 2009. Long-lived volcanism on the lunar farside revealed by SELENE Terrain Camera. Science 323, 905–908. https://doi.org/10.1126/science.1163382.
Head, J.W., 1976. Lunar volcanism in space and time. Rev. Geophys. 14, 265–300. https://doi.org/10.1029/RG014i002p00265.
Head III, J.W., Adams, J.B., McCord, T.B., Pieters, C.M., Zisk, S.H., 1978. Regional stratigraphy and geologic history of Mare Crisium. In: Merrill, R.B., Papike, J.J. (Eds.), Mare Crisium: The View from Luna 24. Pergamon, New York, pp. 43–74.
Head, J.W., Wilson, L., 1992. Lunar mare volcanism: stratigraphy, eruption conditions, and the evolution of secondary crusts. Geochim. Cosmochim. Acta 56 (6), 2155–2175. https://doi.org/10.1016/0016-7037(92)90183-J.
Head, J.W., Wilson, L., 2017. Generation, ascent and eruption of magma on the Moon: new insights into source depths, magma supply, intrusions and effusive/explosive

eruptions (part 2: predicted emplacement processes and observations). Icarus 283, 176–223. https://doi.org/10.1016/j.icarus.2016.05.031.
Head, J.W., Wilson, L., Hiesinger, H., van der Bogert, C., Chen, Y., Dickson, J.L., Ziyuan, O., 2023. Lunar mare basaltic volcanism: volcanic features and emplacement processes. Rev. Mineral. Geochem. 89 (1), 453–507. https://doi.org/10.2138/rmg.2023.89.11.
Hiesinger, H., Head, J.W., 2006. New views of the Moon: an introduction and overview. In: New Views of the Moon, pp. 1–82. https://doi.org/10.1515/9781501509537-005.
Hiesinger, H., Head, J.W., Wolf, U., Jaumann, R., Neukum, G., 2002. Lunar mare basalt flow units: thicknesses determined from crater size-frequency distributions. Geophys. Res. Lett. 29 (8). https://doi.org/10.1029/2002GL014847.
Hiesinger, H., Head, J.W., Wolf, U., Jaumann, R., Neukum, G., 2003. Ages and stratigraphy of mare basalts in Oceanus Procellarum, Mare Nubium, Mare Cognitum, and Mare Insularum. J. Geophys. Res. Planets 108. https://doi.org/10.1029/2002JE001985.
Hiesinger, H., Head III, J.W., Wolf, U., Jaumann, R., Neukum, G., 2006. New ages for basalts in Mare Fecunditatis based on crater size-frequency measurements. In: 37th Lunar Planet. Sci. Conf. Lunar and Planetary Institute, Houston. Texas abstract #1151.
Hiesinger, H., Head, J.W., Wolf, U., Jaumann, R., Neukum, G., 2011a. Ages and stratigraphy of lunar mare basalts: a synthesis. Geol. Soc. Am. Spec. Pap. 477, 1–51. https://doi.org/10.1130/2011.2477(01).
Hiesinger, H., Jaumann, R., Neukum, G., Head III, J.W., 2000. Ages of mare basalts on the lunar nearside. J. Geophys. Res. 105, 29239–29275. https://doi.org/10.1029/2000JE001244.
Hiesinger, H., van der Bogert, C.H., Reiss, D., Robinson, M.S., 2011b. Crater size-frequency distribution measurements of Mare Crisium. In: 42nd Lunar Planet. Sci. Conf. Lunar and Planetary Institute, Houston abstract #2179.
Jin, L., et al., 2025. Global picture of lunar basalt chronology based on the automatic classification of craters. J. Geophys. Res. 130 (10), e2025JE008965. https://doi.org/10.1029/2025JE008965.
Kneissl, T., van Gasselt, S., Neukum, G., 2011. Map-projection-independent crater size-frequency determination in GIS environments—new software tool for ArcGIS. Planet. Space Sci. 59, 1243–1254. https://doi.org/10.1016/j.pss.2010.03.015.
Lemelin, M., Lucey, P.G., Gaddis, L.R., Hare, T., Ohtake, M., 2016. Global map products from the Kaguya Multiband Imager at 512 ppd: minerals, FeO, and OMAT. In: Lunar and Planetary Sci Conf, 47, p. 2994.
Lemelin, M., Lucey, P.G., Miljković, K., Gaddis, L.R., Hare, T., Ohtake, M., 2019. The compositions of the lunar crust and upper mantle: spectral analysis of the inner rings of lunar impact basins. Planet. Space Sci. 165, 230–243. https://doi.org/10.1016/j.pss.2018.10.003.
Lemelin, M., Lucey, P.G., Song, E., Taylor, G.J., 2015. Lunar central peak mineralogy and iron content using the Kaguya Multiband Imager: reassessment of the compositional structure of the lunar crust. J. Geophys. Res. 120, 869–887. https://doi.org/10.1002/2014JE004778.
Lena, R., Wöhler, C., Bregante, M.T., Lazzarotti, P., Lammel, S., 2008. Lunar domes in Mare Undarum: spectral and morphometric properties, eruption conditions, and mode of emplacement. Planet. Space Sci. 56, 553–569. https://doi.org/10.1016/j.pss.2007.11.010.
Li, C., et al., 2022. Characteristics of the lunar samples returned by the Chang'E-5 mission. Natl. Sci. Rev. 9, nwab188. https://doi.org/10.1093/nsr/nwab188.
Li, C., et al., 2024. Nature of the lunar far-side samples returned by the Chang'E-6 mission. Natl. Sci. Rev. 11, nwae328. https://doi.org/10.1093/nsr/nwae328.
Li, Q.-L., et al., 2021. Two-billion-year-old volcanism on the Moon from Chang'e-5 basalts. Nature 600, 54–58. https://doi.org/10.1038/s41586-021-04100-2.
Ling, Z., et al., 2015. Correlated compositional and mineralogical investigations at the Chang'e-3 landing site. Nat. Commun. 6, 8880. https://doi.org/10.1038/ncomms9880.
Lu, X., Cao, H., Ling, Z., Fu, X., Qiao, L., Chen, J., 2021. Geomorphology, mineralogy, and geochronology of mare basalts and non-mare materials around the lunar Crisium basin. Remote Sens. 13, 4828. https://doi.org/10.3390/rs13234828.
Lucey, P., et al., 2006. Understanding the lunar surface and space-Moon interactions. Rev. Mineral. Geochem. 60, 83–219. https://doi.org/10.2138/rmg.2006.60.2.
Lucey, P.G., 2004. Mineral maps of the moon. Geophys. Res. Lett. 31. https://doi.org/10.1029/2003GL019406.
Lucey, P.G., Blewett, D.T., Jolliff, B.L., 2000. Lunar iron and titanium abundance algorithms based on final processing of Clementine ultraviolet-visible images. J. Geophys. Res. 105, 20297–20305. https://doi.org/10.1029/1999JE001117.
McEwen, A.S., Bierhaus, E.B., 2006. The importance of secondary cratering to age constraints on planetary surfaces. Annu. Rev. Earth Planet. Sci. 34, 535–567. https://doi.org/10.1146/annurev.earth.34.031405.125018.
Melosh, H., 1989. Impact cratering: a geologic process. In: Oxford Monographs on Geology and Geophysics. Oxford University Press, London.
Michael, G., Neukum, G., 2010. Planetary surface dating from crater size–frequency distribution measurements: partial resurfacing events and statistical age uncertainty. Earth Planet. Sci. Lett. 294, 223–229. https://doi.org/10.1016/j.epsl.2009.12.041.
Michael, G.G., Kneissl, T., Neesemann, A., 2016. Planetary surface dating from crater size-frequency distribution measurements: Poisson timing analysis. Icarus 277, 279–285. https://doi.org/10.1016/j.icarus.2016.05.019.
Morota, T., et al., 2009. Mare volcanism in the lunar farside Moscoviense region: implication for lateral variation in magma production of the Moon. Geophys. Res. Lett. 36. https://doi.org/10.1029/2009GL040472.
Morota, T., et al., 2011. Timing and characteristics of the latest mare eruption on the Moon. Earth Planet. Sci. Lett. 302, 255–266. https://doi.org/10.1016/j.epsl.2010.12.028.
Nelson, D.M., et al., 2014. Mapping lunar maria extents and lobate scarps using LROC image products. Lunar Planet. Sci. Conf. 45, 2861.
Neukum, G., 1983. Meteoritenbombardement und datierung planetarer oberflachen. In: Habilitation Dissertation for Faculty Membership, Ludwig-Maximilians-Univ..
Neukum, G., Ivanov, B.A., 1994. Crater size distributions and impact probabilities on Earth from lunar, terrestrial-planet, and asteroid cratering data. In: Hazards due to Comets and Asteroids, pp. 359–416.
Neukum, G., Ivanov, B.A., Hartmann, W.K., 2001. Cratering records in the inner solar system in relation to the lunar reference system. Space Sci. Rev. 96, 55–86. https://doi.org/10.1023/A:1011989004263.
Neumann, G.A., et al., 2015. Lunar impact basins revealed by Gravity Recovery and Interior Laboratory measurements. Sci. Adv. 1, e1500852. https://doi.org/10.1126/sciadv.1500852.
Nunes, P.D., Tatsumoto, M., Unruh, D.M., 1974. U-Th-Pb systematics of some Apollo 17 lunar samples and implications for a lunar basin excavation chronology. In: Proceedings of the Fifth Lunar Science Conference, 2, pp. 1487–1514.
Nyquist, L.E., Shih, C.-Y., 1992. The isotopic record of lunar volcanism. Geochim. Cosmochim. Acta 56, 2213–2234. https://doi.org/10.1016/0016-7037(92)90185-L.
Orgel, C., et al., 2018. Ancient bombardment of the inner solar system: reinvestigation of the "fingerprints" of different impactor populations on the lunar surface. J. Geophys. Res. Planet. 123, 748–762. https://doi.org/10.1002/2017JE005451.
Otake, H., Ohtake, M., Hirata, N., 2012. Lunar iron and titanium abundance algorithms based on SELENE (Kaguya) multiband imager data. In: 43rd Lunar and Planetary Science Conference. Lunar and Planetary Institute, The Woodlands, Texas abstract #1905.
Papike, J.J., Hodges, F.N., Bence, A.E., Cameron, M., Rhodes, J.M., 1976. Mare basalts: crystal chemistry, mineralogy, and petrology. Rev. Geophys. 14, 475–540. https://doi.org/10.1029/RG014i004p00475.
Pasckert, J.H., Hiesinger, H., van der Bogert, C.H., 2015. Small-scale lunar farside volcanism. Icarus 257, 336–354. https://doi.org/10.1016/j.icarus.2015.04.040.
Pasckert, J.H., Hiesinger, H., van der Bogert, C.H., 2018. Lunar farside volcanism in and around the South Pole–Aitken basin. Icarus 299, 538–562. https://doi.org/10.1016/j.icarus.2017.07.023.
Qian, Y., Xiao, L., Head, J.W., van der Bogert, C.H., Hiesinger, H., Wilson, L., 2021. Young lunar mare basalts in the Chang'e-5 sample return region, northern Oceanus Procellarum. Earth Planet. Sci. Lett. 555, 116702. https://doi.org/10.1016/j.epsl.2020.116702.
Qiao, L., Ling, Z., Fu, X., Li, B., 2019. Geological characterization of the Chang'e-4 landing area on the lunar farside. Icarus 333, 37–51. https://doi.org/10.1016/j.icarus.2019.05.029.
Rajmon, D., Spudis, P., 2000. Geology and stratigraphy of Mare Fecunditatis. In: Lunar and Planetary Science Conference, p. 1913.
Righter, K., Drake, M.J., 2000. Metal/silicate equilibrium in the early earth—new constraints from the volatile moderately siderophile elements Ga, Cu, P, and Sn. Geochim. Cosmochim. Acta 64, 3581–3597. https://doi.org/10.1016/S0016-7037(00)00466-X.
Robbins, S.J., Hynek, B.M., 2012. A new global database of Mars impact craters ≥1 km: 1. Database creation, properties, and parameters. J. Geophys. Res. Planet. 117, E05004. https://doi.org/10.1029/2011JE003966.
Robbins, S.J., Riggs, J.D., Weaver, B.P., Bierhaus, E.B., Chapman, C.R., Kirchoff, M.R., Singer, K.N., Gaddis, L.R., 2018. Revised recommended methods for analyzing crater size-frequency distributions. Meteorit. Planet. Sci. 53, 891–931. https://doi.org/10.1111/maps.12990.
Schaeffer, O.A., Husain, L., 1974. Chronology of lunar basin formation. Proc. Lunar Sci. Conf. 5, 1541–1555.
Shearer, C., Papike, J., 1999. Magmatic evolution of the Moon. Am. Mineral. 84, 1469–1494. https://doi.org/10.2138/am-1999-1001.
Shearer, C.K., et al., 2006. Thermal and magmatic evolution of the Moon. Rev. Mineral. Geochem. 60, 365–518. https://doi.org/10.2138/rmg.2006.60.4.
Shi, X., et al., 2026. Refined lunar global chemistry mapping using farside ground truth information gathered by Chang'e-6. Nat. Sensors 1, 232–240. https://doi.org/10.1038/s44460-025-00021-z.
Smith, D.E., et al., 2010. The lunar orbiter laser altimeter investigation on the lunar reconnaissance orbiter mission. Space Sci. Rev. 150, 209–241. https://doi.org/10.1007/s11214-009-9512-y.
Snape, J.F., Nemchin, A.A., Whitehouse, M.J., Merle, R.E., Hopkinson, T., Anand, M., 2019. The timing of basaltic volcanism at the Apollo landing sites. Geochim. Cosmochim. Acta 266, 29–53. https://doi.org/10.1016/j.gca.2019.07.042.
Solomon, S.C., Head, J.W., 1980. Lunar mascon basins: lava filling, tectonics, and evolution of the lithosphere. Rev. Geophys. 18, 107–141. https://doi.org/10.1029/RG018i001p00107.
Speyerer, E.J., Robinson, M.S., Denevi, B.W., LROC Team, 2011. Lunar reconnaissance orbiter camera global morphological map of the Moon. Lunar Planet. Sci. Conf. 42, 2387.
Spudis, P., Hawke, B., Lucey, P., 1989. The lunar Crisium basin: geology, rings, and deposits. In: Abstracts of the Lunar and Planetary Science Conference, 20, p. 1042.
Stöffler, D., Ryder, G., 2001. Stratigraphy and isotope ages of lunar geologic units: chronological standard for the inner solar system. Space Sci. Rev. 96, 9–54. https://doi.org/10.1023/A:1011937020193.
Stöffler, D., Ryder, G., Ivanov, B.A., Artemieva, N.A., Cintala, M.J., Grieve, R.A., 2006. Cratering history and lunar chronology. Rev. Mineral. Geochem. 60, 519–596. https://doi.org/10.2138/rmg.2006.60.05.
Taylor, L.A., et al., 2010. Mineralogical and chemical characterization of lunar highland soils: insights into the space weathering of soils on airless bodies. J. Geophys. Res. 115. https://doi.org/10.1029/2009JE003427.

Taylor, L.A., Pieters, C.M., Keller, L.P., Morris, R.V., McKay, D.S., 2001. Lunar mare soils: space weathering and the major effects of surface-correlated nanophase Fe. J. Geophys. Res. 106, 27985–27999. https://doi.org/10.1029/2000JE001402.

Terada, K., Anand, M., Sokol, A.K., Bischoff, A., Sano, Y., 2007. Cryptomare magmatism 4.35 Gyr ago recorded in lunar meteorite Kalahari 009. Nature 450, 849–852. https://doi.org/10.1038/nature06356.

Tian, H.-C., et al., 2021. Non-KREEP origin for Chang'e-5 basalts in the Procellarum KREEP Terrane. Nature 600, 59–63. https://doi.org/10.1038/s41586-021-04119-5.

Trieloff, M., Deutsch, A., Jessberger, E.K., 1998. The age of the Kara impact structure, Russia. Meteorit. Planet. Sci. 33, 361–372. https://doi.org/10.1111/j.1945-5100.1998.tb01640.x.

Vaniman, D., Papike, J., 1977. Ferrobasalts from Mare Crisium: Luna 24. Geophys. Res. Lett. 4, 497–500. https://doi.org/10.1029/GL004i010p00497.

Wang, C., et al., 2025a. The source and thermal driver of young (< 3.0 Ga) lunar volcanism. Sci. Adv. 11, eadv9085. https://doi.org/10.1126/sciadv.adv9085.

Wang, Z., et al., 2025b. Chemical compositions of Chang'e-6 lunar soil and substantial addition of noritic crust ejecta from Apollo basin. Geology 53, 557–561. https://doi.org/10.1130/G53086.1.

Whitten, J., et al., 2011. Lunar mare deposits associated with the Orientale impact basin: new insights into mineralogy, history, mode of emplacement, and relation to Orientale Basin evolution from Moon Mineralogy Mapper (M3) data from Chandrayaan-1. J. Geophys. Res. 116. https://doi.org/10.1029/2010JE003736.

Wichman, R., Schultz, P., 1995. Floor-fractured craters in Mare Smythii and west of Oceanus Procellarum: implications of crater modification by viscous relaxation and igneous intrusion models. J. Geophys. Res. 100, 21201–21218. https://doi.org/10.1029/95JE02297.

Wieczorek, M.A., et al., 2013. The crust of the Moon as seen by GRAIL. Science 339, 671–675. https://doi.org/10.1126/science.1231530.

Wilhelms, D.E., 1987. The geologic history of the moon. In: U.S. Geological Survey Professional Paper 1348, U.S. Geological Survey, Washington, DC. https://doi.org/10.3133/pp1348.

Xiao, Z., Strom, R.G., 2012. Problems determining relative and absolute ages using the small crater population. Icarus 220, 254–267. https://doi.org/10.1016/j.icarus.2012.05.012.

Yang, M.-H., et al., 2025. 2.2-billion-year-old KREEP-rich volcanism on the Moon. Sci. Bull. https://doi.org/10.1016/j.scib.2025.08.032.

Zhang, Q.W., et al., 2025. Lunar farside volcanism 2.8 billion years ago from Chang'e-6 basalts. Nature 643, 356–360. https://doi.org/10.1038/s41586-024-08382-0.

Zhao, S., et al., 2022. Lunar mare Fecunditatis: a science-rich region and a concept mission for long-distance exploration. Remote Sens. 14, 1062. https://doi.org/10.3390/rs14051062.